An Indirect Model Predictive Control Method for Grid-Connected Three-Level Neutral Point Clamped Converters with LCL Filters

Mattia Rossi, *Member, IEEE,* Petros Karamanakos, *Senior Member, IEEE,*
and Francesco Castelli-Dezza, *Member, IEEE*

***Abstract*—This paper presents a model predictive control (MPC) algorithm for a three-level neutral point clamped converter connected to the grid via an LCL filter. The proposed long-horizon MPC method, formulated as a multi-criterion quadratic program (QP), simultaneously controls the grid and converter current as well as the filter capacitor voltage, while meeting the relevant grid standards. To achieve the latter, a carrier-based pulse width modulation (CB-PWM) stage is employed. Finally, soft constraints are included to ensure operation of the system within its safe operating limits, particularly with regards to a potential overcurrent or overvoltage trip during transient operation. The presented simulation results based on a medium-voltage system as well as experimental studies based on a scaled-down prototype verify the effectiveness of the proposed method.**

***Index Terms*—Grid-connected power converters, model predictive control (MPC), optimal control, quadratic programming, multiple-input multiple-output (MIMO) control, constraints.**

I. Introduction

GRID-TIED converters are a key technology for the integration of renewable energy sources, scalable loads, and high-performance drives in the electrical grid. For medium-voltage (MV) applications, grid codes—such as the IEEE 519 [1] and the IEC 61000-2-4 [2] standards—impose tight limits on the amplitudes of the current and voltage harmonics injected at the point of common coupling (PCC). To this end, LCL filters are commonly used to interface the converters with the grid as they provide stronger harmonic attenuation along with a reduced size (i.e., lower cost) compared with, e.g., L filters. The LCL filter, however, introduces additional control challenges due to the higher order of the resulting system, i.e., besides the control of the grid current, the control of the converter current and capacitor voltage are needed. Moreover, the resonance introduced by the filter needs to be adequately damped to avoid current harmonics amplification, or, even, stability issues [3].

To tackle the above control tasks, conventional control solutions, such as voltage oriented control (VOC) and its derivatives [4], employ cascaded control structures that are designed based on linear control principles. Furthermore, since they mask the switching nature of the power electronic system, a pulse width modulation (PWM) stage is employed to translate the modulating signal into switching commands [5]. Such control schemes, however, tend to perform poorly when operation at low switching frequencies is required—as is the case of MV power electronic systems—especially during transients, due to insufficient decoupling of the control loops. To achieve higher bandwidth, direct control methods, i.e., controllers without a dedicated modulator, can be employed, e.g., the so-called direct power control (DPC) and its derivatives [6]–[8]. The grid current produced with these control strategies, however, tends to violate the grid standards as the lack of a modulator gives rise to pronounced harmonic distortions. Moreover, regardless of the adopted control strategy, it is typical for conventional control schemes to be augmented with an active damping mechanism, e.g., filter-based active damping [9], or a virtual resistance [10]. Hence, to achieve a favorable operation during both steady-state and transient conditions, more sophisticated control algorithms are required, such as model predictive control (MPC).

During the last decade, MPC has gained popularity in the field of power electronics as a promising alternative to traditional control and modulation strategies [11]–[13]. Depending on whether a modulator is used or not, MPC is classified into two categories, i.e., direct MPC—also known as finite control set MPC (FCS-MPC)—and indirect MPC—also referred to as continuous control set MPC (CCS-MPC) [14]. FCS-MPC performs the control and modulation tasks in one computational stage, thus it directly generates the optimal switching signals. This implies that the controller operates the converter at a variable switching frequency, which results in non-deterministic harmonic spectra [15]. For grid-tied converters with filters, this complicates the system design, e.g., it may lead to an overly conservative choice for the output filter, cooling system, and semiconductor devices, while meeting the grid standards becomes challenging [16].

Due to the above reasons, a preferred choice is to use MPC with a modulator, such as carrier-based PWM (CB-PWM) or space vector modulation (SVM) [17]. In this direction, a few works, such as [18]–[22], introduced MPC-based approaches with a dedicated modulation stage. However, works like [19] do not account for the intrinsic multiple-input multiple-output (MIMO) nature of the power electronic system, thus resulting in inferior performance. As for [18], [20]–[22], even though they proposed MIMO MPC-based schemes, they do not introduce system (i.e., state/output) constraints that enable the controller to ensure hardware protection and avoid converter trip levels. Moreover, it is noteworthy that [18], [20] do not introduce input constraints that would allow operation in overmodulation, meaning that they are not able to fully

M. Rossi and P. Karamanakos are with the Faculty of Information Technology and Communication Sciences, Tampere University, 33101 Tampere, Finland, e-mail: mattia.rossi@tuni.fi, p.karamanakos@ieee.org.

F. Castelli-Dezza is with the Department of Mechanical Engineering, Politecnico di Milano, 20156 Milan, Italy, e-mail: francesco.castelli dezza@polimi.it

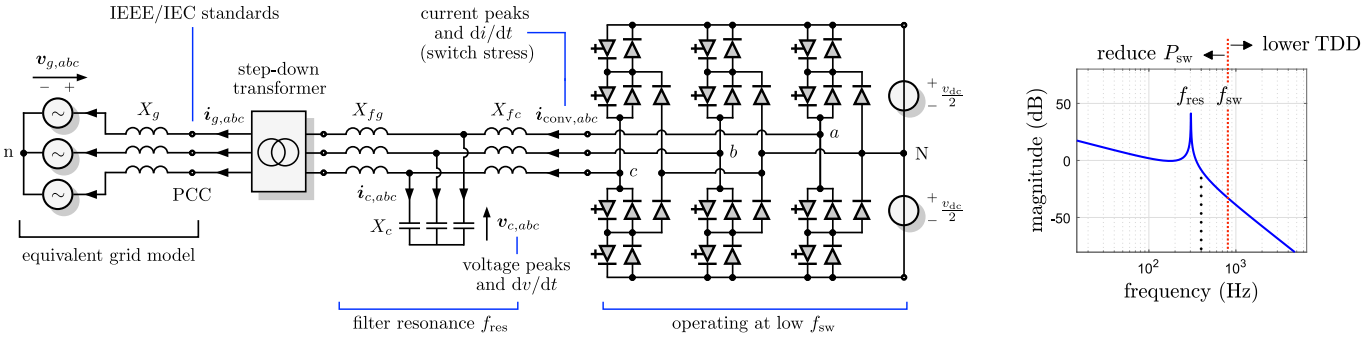

(a) (b)

Fig. 1. (a) Grid-tied 3L-NPC converter, based on IGCTs, with an LCL filter. The potential root cause of faults is also highlighted. (b) Frequency response of the LCL filter. The filter resonance f_{res} and switching frequency f_{sw} are shown. The latter should be as low as possible, while keeping the system stability.

utilize the available dc-link voltage. Finally, the only methods experimentally tested, namely [18] and [21], have a short prediction horizon to keep the computational complexity low. In doing so, however, a sufficient degree of active damping is not achieved, meaning that the filter has to be oversized so that its resonance frequency is not excited.

Motivated by the above, this paper considers an indirect MPC for a three-level neutral point clamped (3L-NPC) converter connected to the grid via an LCL filter.[1] By employing a CB-PWM stage the converter can be operated at a fixed switching frequency and generate deterministic harmonic spectra, with harmonic components limited to non-triplen odd integer multiplies of the fundamental frequency. Furthermore, by formulating the optimization problem underlying indirect MPC as a multi-criterion quadratic program (QP) several benefits follow. First, all primary control objectives, i.e., the control of the grid and converter current as well as of the filter capacitor voltage, are achieved and the relevant grid codes met, while the converter is operated at low switching frequency.

Second, the computational complexity of the problem remains moderate, even when long horizons are utilized for improved system performance [24]. Regarding the latter, it is worth mentioning that they are particularly beneficial when higher-order systems—as the examined one—are of concern, see, e.g., [25], since it has been manifested that—when combined with full-state information—they can provide active damping without the need for additional damping loops. This implies a simpler controller structure, as opposed to conventional control schemes, where passive or active damping is necessary to rein in the filter resonance.

An additional important advantage of the proposed control scheme is that explicit constraints are taken into account in the optimization problem. Specifically, hard constraints are imposed on the control input (i.e., the modulating signal) and soft constraints on the system output to ensure operation within the safe operating area—given as trip levels—of the system. Hence, damage (or aging) of the hardware due to overvoltages and/or overcurrents can be avoided (reduced). It is worth mentioning that this feature stands in stark contrast to conventional control solutions in grid applications, see, e.g., [4]–[9], [26].

[1]This paper is an extension of [23]. Herein, as compared with [23], a deeper theoretical analysis of the proposed method is presented along with its experimental verification based on a scaled-down prototype.

Finally, owing to the QP formulation of the optimization problem, online solvers that are able to solve such problems on embedded hardware in a manner of microseconds, see, e.g., [27]–[29], can be employed, thus facilitating the real-time implementation of the controller. Moreover, since the adoption of a feasible and effective embedded MPC implementation is of great importance, the computational burden of the proposed algorithm is carefully evaluated in terms of execution time, number of iterations and solution accuracy. In doing so, insight into the real-time certification of the code is provided.

This paper is structured as follows. The case study in consideration is presented in Section II. The model of the system that serves as the prediction model is derived in Section III, while the introduction of the proposed MPC algorithm and its formulation as a QP are given in Section IV. In Section V, the performance of the MPC strategy is demonstrated for the chosen case study based on simulations. Moreover, the factors that affect the closed-loop performance are analyzed in Section VI. Section VII presents real-time implementation issues along with the subsequent experimental studies based on a scaled-down prototype. Finally, conclusions are drawn in Section VIII.

II. Case Study

Consider the three-phase 3L-NPC converter connected to the grid via an intermediate LCL filter, as shown in Fig. 1(a). The filter is placed between the converter and the step-down transformer in order to reduce the harmonic distortions at the PCC. The voltage $\boldsymbol{v}_{g,abc}(t)$ to the left of the PCC models the grid source, while $\boldsymbol{i}_{g,abc}(t)$ is the grid current. The distribution lines are approximated by the grid resistance R_g and inductance L_g, which are assumed equal for all phases. The grid reactance is $X_g = \omega_g L_g$, where ω_g is the grid angular frequency. Likewise, the step-down transformer can be represented by its split series resistance R_t and leakage reactance X_t. The LCL filter is described by the grid-side resistance R_{fg} and reactance X_{fg}, the capacitor reactance[2] X_c and its internal resistance R_c as well as the converter-side resistance R_{fc} and reactance X_{fc}. The converter current is $\boldsymbol{i}_{\text{conv},abc}(t)$, $\boldsymbol{i}_{c,abc}(t)$ is the current flowing through the filter capacitor branch, while $\boldsymbol{v}_{c,abc}(t)$ is the capacitor voltage.[3]

[2]Strictly speaking, X_c denotes the inverse of the reactance.

[3]Note that currents flowing towards the grid are assumed to be positive.

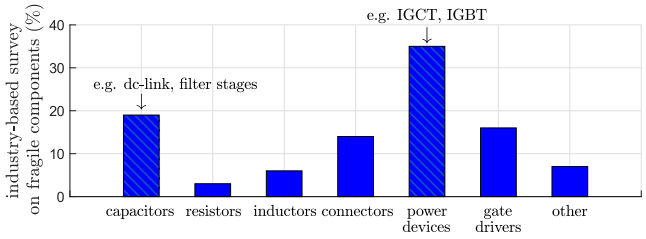

Fig. 2. Distribution (in percentage) of industry responses to the question "What is the most fragile component of your power electronic-based systems?" according to the dataset given in [30].

To keep the demonstration of the proposed method simple, the dc-link voltage is assumed to be constant $v_{\rm dc}(t) = V_{\rm dc}$ and balanced, thus, the neutral point potential N is fixed at zero. Since additional loads may be connected to the PCC, strict grid standards are imposed at this point. The IEEE 519 [1] and IEC 61000-2-4 [2] standards are considered in this paper. In addition, physical limitations, such as voltage peaks and $\mathrm{d}v/\mathrm{d}t$ across the filter capacitor as well as current peaks and $\mathrm{d}i/\mathrm{d}t$ of the converter current (i.e., through the semiconductors) are considered and converter trip levels defined [30]. Moreover, given the MV target, the converter is required to operate at a low switching frequency and as close to the resonance frequency of the LCL filter as possible (see Fig. 1(b)), without exciting the current harmonics close to the latter. In doing so, not only the power switching losses can be kept low, but also the produced grid current harmonics can abide by the aforementioned grid standards, and potential stability issues avoided, while increasing the system reliability.

A. Grid Strength and LCL Filter Resonance

The grid strength is characterized by the impedance ratio $k_{\rm XR}$ and the short-circuit ratio $k_{\rm sc}$, which are defined as

$$k_{\rm XR} = \frac{X_g}{R_g}\,, \quad k_{\rm sc} = \frac{S_{\rm sc}}{S_R} = \frac{V_R^2}{\sqrt{R_g^2 + X_g^2}}\frac{1}{S_R}\,, \tag{1}$$

where S_R is the rated apparent power. The short-circuit power $S_{\rm sc}$ can be interpreted as the maximum power that the grid can provide to the PCC. According to the system parameters in Table I, ratios of $k_{\rm sc} \approx 19.96$ and $k_{\rm XR} \approx 10.02$ indicate a strong grid where the impedance seen at the PCC dominates over the grid impedance [13].

By lumping the resistances and reactances to the left of the LCL filter into the quantities $R = R_g + R_t + R_{fg}$ and $X = X_g + X_t + X_{fg}$ the filter resonances are defined as

$$f_{\rm res} = f_B \frac{1}{\sqrt{X_c \frac{X_{fc} X}{X_{fc}+X}}}\,, \quad \widetilde{f}_{\rm res} = f_B \frac{1}{\sqrt{X_c X}}\,, \tag{2}$$

where f_B is the base frequency. As shown in Fig. 1(b), the dominant one is $f_{\rm res}$, resulting by the interaction of the filter capacitor reactance X_c with the converter-side filter reactance X_{fc} and the equivalent total reactance X. The three resistors R, R_c and R_{fc} can be assumed negligible and, thus, they effectively provide no passive damping. Given the dominant resonance frequency $f_{\rm res}$, a controller should avoid its excitation such that potential stability problems are avoided.

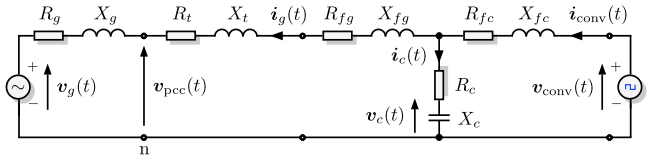

Fig. 3. Equivalent circuit (harmonic model) in the $\alpha\beta$-plane of the conversion scheme given in Fig. 1(a). The PCC is denoted by the voltage $\boldsymbol{v}_{\rm pcc}(t)$.

B. Reliability

The industry-based survey in [30] summarizes the impact of operating conditions on the reliability of components used in power converters ranging from low ($< 50\,$kW) to high power ($> 0.5\,$MW). Given the failure distribution shown in Fig. 2, power semiconductor devices and filter capacitor banks (e.g., film capacitors in LCL filters) are ranked as two of the most fragile elements in high power electronic systems.

The main failure root causes are the operating environment (e.g., ambient temperature and moisture at commissioning location), transients (i.e., voltage/current swell or unbalances), or heavy/long overloads operation. In particular, sudden power transients may lead to overcurrents and/or overvoltages that may cause insulation damage or breaking of the power electronic system components, while long overloads can result in significant thermal stress in the devices. As a result, such adverse operating conditions can potentially lead to a trip of the converter or interruption of its operation [31]. For this reason, safety limits (i.e., trip levels) are required to prevent the degradation and/or failure of the components that may lead to a trip of the system.

III. Controller Model

In the sequel, a mathematical description of the converter dynamics is derived in the $\alpha\beta$-reference frame. All variables given in the abc-plane $\boldsymbol{\xi}_{abc} = [\xi_a\ \xi_b\ \xi_c]^T$ are mapped into two-dimensional vectors $\boldsymbol{\xi}_{\alpha\beta} = [\xi_\alpha\ \xi_\beta]^T$ via the reduced Clarke transformation matrix $\boldsymbol{K}$ (i.e., without the common-mode component)

$$\boldsymbol{K} = \frac{2}{3}\begin{bmatrix} 1 & -\frac{1}{2} & -\frac{1}{2} \\ 0 & \frac{\sqrt{3}}{2} & -\frac{\sqrt{3}}{2} \end{bmatrix}. \tag{3}$$

Based on Fig. 1(a), the equivalent circuit of the system in consideration is derived in the $\alpha\beta$-plane.[4] Before doing so, all SI variables are normalized based on the rated values of the secondary side of the step-down transformer.[5]

Since an indirect MPC approach is proposed in this paper, it is implied that the controller output is the three-phase modulating signal $\boldsymbol{u}_{{\rm ref},abc}(t) = [u_{{\rm ref},a}\ u_{{\rm ref},b}\ u_{{\rm ref},c}]^T \in \boldsymbol{\mathcal{U}} = [-1,1]^3 \subset \mathbb{R}^3$. This relates to the ideal converter voltage $\boldsymbol{v}_{{\rm conv,ref}}(t)$ via

$$\boldsymbol{v}_{{\rm conv,ref}}(t) = \frac{V_{\rm dc}}{2}\boldsymbol{K}\boldsymbol{u}_{{\rm ref},abc}(t) = \frac{V_{\rm dc}}{2}\boldsymbol{u}_{\rm ref}(t)\,, \tag{4}$$

[4]Hereafter, to simplify the notation, the subscript $\alpha\beta$ is dropped from all vectors unless otherwise stated.

[5]According to Table I, the per unit (p.u.) system is established using the base quantities $V_B = \sqrt{2/3}V_R$, $I_B = \sqrt{2}I_R$, $S_B = S_R = (3/2)\,V_B I_B$, and $\omega_B = \omega_g = 2\pi f_g$, where V_R, I_R, and S_R denote the (rated) rms line-to-line voltage, rms line current, and apparent power, respectively, referred to the secondary side of the transformer.

while, the actual converter voltage $\boldsymbol{v}_{\mathrm{conv}}(t)$ approximates $\boldsymbol{v}_{\mathrm{conv,ref}}(t)$ through the 3L CB-PWM principle. A phase disposition (PD) approach is considered in this paper because it results in lower harmonic distortions, see [17].

Given the equivalent circuit in Fig. 3, the system dynamics in the $\alpha\beta$-plane are given by the following continuous-time differential equations

$$X_{fc}\frac{\mathrm{d}\boldsymbol{i}_{\mathrm{conv}}(t)}{\mathrm{dt}} = -R_1\boldsymbol{i}_{\mathrm{conv}}(t) - \boldsymbol{v}_c(t) + R_c\boldsymbol{i}_g(t) + \boldsymbol{v}_{\mathrm{ref}}(t) \quad (5a)$$

$$X_c\frac{\mathrm{d}\boldsymbol{v}_c(t)}{\mathrm{dt}} = \boldsymbol{i}_c(t) = \boldsymbol{i}_{\mathrm{conv}}(t) - \boldsymbol{i}_g(t) \quad (5b)$$

$$X\frac{\mathrm{d}\boldsymbol{i}_g(t)}{\mathrm{dt}} = R_c\boldsymbol{i}_{\mathrm{conv}}(t) + \boldsymbol{v}_c(t) - R_2\boldsymbol{i}_g(t) - \boldsymbol{v}_g(t) \quad (5c)$$

$$\frac{\mathrm{d}\boldsymbol{v}_g(t)}{\mathrm{dt}} = \omega_g\begin{bmatrix}0 & -1\\ 1 & 0\end{bmatrix}\boldsymbol{v}_g(t)\,. \quad (5d)$$

Note that the above expression is derived on the assumption of a symmetrical balanced three-phase grid. Moreover, $R_1 = R_{fc} + R_c$ and $R_2 = R + R_c$ are introduced for notational simplification, while $\boldsymbol{v}_{\mathrm{conv,ref}}(t)$ is simply called $\boldsymbol{v}_{\mathrm{ref}}(t)$.

By defining $\boldsymbol{x}(t) = [\boldsymbol{i}_{\mathrm{conv}}^T(t)\ \boldsymbol{v}_c^T(t)\ \boldsymbol{i}_g^T(t)\ \boldsymbol{v}_g^T(t)]^T \in \mathbb{R}^8$, and $\boldsymbol{y}(t) = [\boldsymbol{i}_{\mathrm{conv}}^T(t)\ \boldsymbol{v}_c^T(t)\ \boldsymbol{i}_g^T(t)]^T \in \mathbb{R}^6$ as the state and output vectors, respectively, and $\boldsymbol{u}(t) = \boldsymbol{u}_{\mathrm{ref},abc}(t)$ as the control input (i.e., the three-phase modulating signal), the continuous-time state-space representation is

$$\frac{\mathrm{d}\boldsymbol{x}(t)}{\mathrm{dt}} = \boldsymbol{F}\boldsymbol{x}(t) + \boldsymbol{G}\boldsymbol{u}(t) \quad (6a)$$

$$\boldsymbol{y}(t) = \boldsymbol{C}\boldsymbol{x}(t)\,, \quad (6b)$$

where $\boldsymbol{F} \in \mathbb{R}^{8\times8}$, $\boldsymbol{G} \in \mathbb{R}^{8\times3}$, and $\boldsymbol{C} \in \mathbb{R}^{6\times8}$ given by

$$\boldsymbol{F} = \begin{bmatrix} -\frac{R_1}{X_{fc}}\boldsymbol{I}_2 & -\frac{1}{X_{fc}}\boldsymbol{I}_2 & \frac{R_c}{X_{fc}}\boldsymbol{I}_2 & \boldsymbol{0}_{2\times2} \\ \frac{1}{X_c}\boldsymbol{I}_2 & \boldsymbol{0}_{2\times2} & -\frac{1}{X_c}\boldsymbol{I}_2 & \boldsymbol{0}_{2\times2} \\ \frac{R_c}{X}\boldsymbol{I}_2 & \frac{1}{X}\boldsymbol{I}_2 & -\frac{R_2}{X}\boldsymbol{I}_2 & -\frac{1}{X}\boldsymbol{I}_2 \\ \boldsymbol{0}_{2\times2} & \boldsymbol{0}_{2\times2} & \boldsymbol{0}_{2\times2} & \omega_g\begin{bmatrix}0 & -1\\ 1 & 0\end{bmatrix} \end{bmatrix}$$

$$\boldsymbol{G} = \frac{v_{\mathrm{dc}}}{2X_{fc}}\begin{bmatrix}\boldsymbol{I}_2 & \boldsymbol{0}_{2\times6}\end{bmatrix}^T\boldsymbol{K}, \quad \boldsymbol{C} = \begin{bmatrix}\boldsymbol{I}_6 & \boldsymbol{0}_{6\times2}\end{bmatrix}.$$

Note that since an ideal grid is assumed, the amplitude V_g and frequency ω_g of $\boldsymbol{v}_g(t)$ are constant, making $\boldsymbol{F}$ a time-invariant matrix.[6] Moreover, due to the assumption of a constant dc link, $\boldsymbol{G}$ is also time invariant. Finally, the dimensions of the zero $\boldsymbol{0}$ and identity $\boldsymbol{I}$ matrices are given by their subscripts.

MPC requires the prediction model of the system to be in the discrete-time domain. The system dynamics, given by (6), are discretized using exact discretization with the sampling interval T_s. This yields

$$\boldsymbol{x}(k+1) = \boldsymbol{A}\boldsymbol{x}(k) + \boldsymbol{B}\boldsymbol{u}(k) \quad (8a)$$

$$\boldsymbol{y}(k) = \boldsymbol{C}\boldsymbol{x}(k)\,, \quad (8b)$$

with $\boldsymbol{A} = \mathbf{e}^{\boldsymbol{F}T_s}$ and $\boldsymbol{B} = \int_0^{T_s}\mathbf{e}^{\boldsymbol{F}\tau}\,\mathrm{d}\tau\,\boldsymbol{G} = -\boldsymbol{F}^{-1}(\boldsymbol{I}_8 - \boldsymbol{A})\boldsymbol{G}$, since $\boldsymbol{F}$ is nonsingular. Moreover, $\mathbf{e}$ is the matrix exponential, and $k \in \mathbb{N}$ denotes the discrete time step.

[6]Nevertheless, if the grid is subject to voltage imbalances, $\boldsymbol{v}_g(t)$ may be considered as an external disturbance to the system instead of a state. In doing so, $\boldsymbol{F}$ remains time invariant.

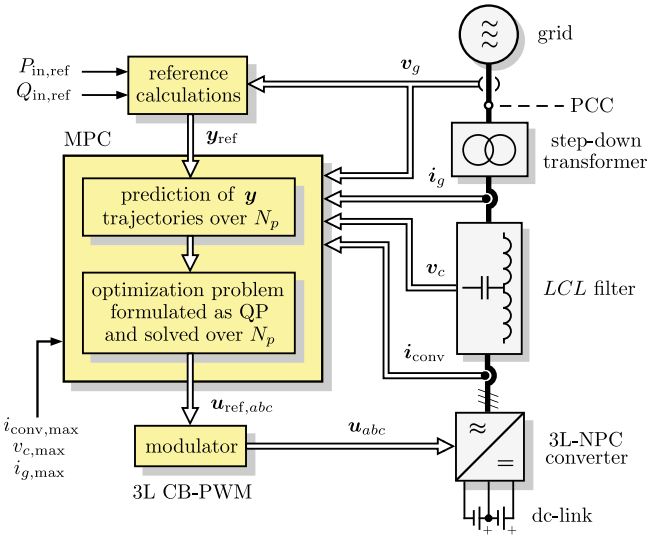

Fig. 4. Indirect MPC formulated as a multi-criterion QP for the ac-dc conversion system shown in Fig. 1(a). The output references are computed from the power demand; a 3L CB-PWM is included.

IV. Long-Horizon Indirect MPC as a QP

To address the control problem of the grid-tied 3L-NPC converter with an LCL filter, an indirect MPC approach is developed that aims to regulate the grid current $\boldsymbol{i}_g(t)$, converter current $\boldsymbol{i}_{\mathrm{conv}}(t)$ and capacitor voltage $\boldsymbol{v}_c(t)$ along their sinusoidal references. These reference values are computed based on the real $P_{\mathrm{in,ref}}(t)$ and reactive $Q_{\mathrm{in,ref}}(t)$ power requirements on the secondary side of the step-down transformer, with $Q_{\mathrm{in,ref}}(t) = 0$ at steady-state operation to achieve unity power factor (i.e., $\mathrm{pf} = 1$). The ultimate goal is to produce a low total demand distortion (TDD) of $\boldsymbol{i}_{g,abc}(t)$ and $\boldsymbol{v}_{\mathrm{pcc},abc}(t)$ as well as limit the amplitude of the associated harmonics to meet the relevant grid standards. Moreover, during power transients, very fast current and voltage responses have to be achieved, while keeping $\boldsymbol{i}_{\mathrm{conv},abc}(t)$ and $\boldsymbol{v}_{c,abc}(t)$ within given bounds, designed as converter trip levels. To this end, soft constraints are implemented to introduce the physical limitations of the switching devices and passive components into the optimization problem so that reliability issues—as described in Section II-B—are avoided.[7] Furthermore, hard constraints are imposed on the modulating signal/control input $\boldsymbol{u}_{\mathrm{ref},abc}(t) = \boldsymbol{u}(t)$ to ensure that its amplitude does not exceed the carrier signals bounds, while still enabling the controller to operate in overmodulation. In doing so, the physical limitations of the system, as imposed by the available dc-link voltage, are always respected and accounted for. Finally, given the MV system in consideration, all objectives should be met while operating the system at low device switching frequency, i.e., f_{sw} of a few hundred hertz, to keep the switching power losses low. The proposed approach is summarized in Fig. 4.

A. Computation of the Output Reference Signals

According to Fig. 4, the reference values of the real and reactive power, $P_{\mathrm{in,ref}}$ and $Q_{\mathrm{in,ref}}$, respectively, are chosen

[7]As the implementation of *hard* constraints on the state/output variables may lead to feasibility issues, soft constraints are typically preferred to maintain feasibility of the optimization problem underlying MPC [32].

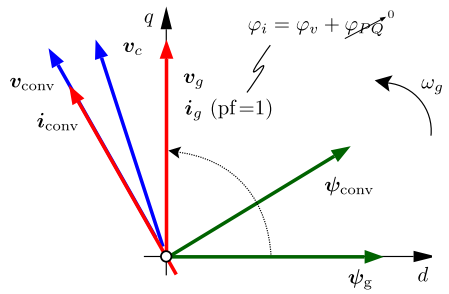

Fig. 5. System variables in the rotating dq-reference frame at steady-state operation assuming unity power factor (pf = 1), which leads to $\varphi_{PQ} = 0$. The reference frame rotates with the grid frequency ω_g.

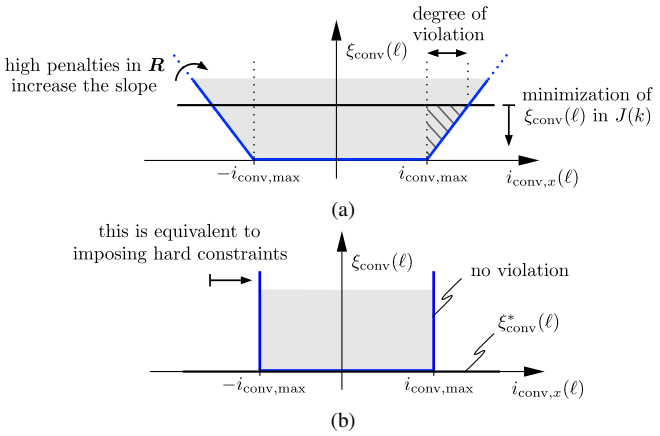

Fig. 6. (a) Example of soft constraints applied on $i_{{\rm conv},a}(\ell)$ at each time step ℓ through the slack variable $\xi_{\rm conv}(\ell)$, for which the feasible space is restricted by the blue lines. The black line denotes the optimal value $\xi^*_{\rm conv}(\ell)$ which is computed by solving the complete optimization problem (22). (b) Effect of a heavy penalization leading to the same behavior as imposing hard constraints.

such that operation under the desired power factor is achieved. These values are used to derive the output reference vector $\boldsymbol{y}_{\rm ref}(k)$ for the inner MPC-based loop. Specifically, $\boldsymbol{y}_{\rm ref}(k)$ consists of the desired values for the converter current $\boldsymbol{i}_{\rm conv,ref}$, filter capacitor voltage $\boldsymbol{v}_{c,\rm ref}$, and grid current $\boldsymbol{i}_{g,\rm ref}$, i.e., $\boldsymbol{y}_{\rm ref} = [\boldsymbol{i}^T_{\rm conv,ref}\ \boldsymbol{v}^T_{c,\rm ref}\ \boldsymbol{i}^T_{g,\rm ref}]^T$, and is computed at each time step k. To do so, the phase of the grid voltage $\varphi_v(t) = \int_0^t \omega_g(\tau)\ {\rm d}\tau + \varphi(0)$ is required. The latter is measured by means of a phase-locked-loop (PLL) and synchronized with the MPC algorithm. With this information, the phase of the reference grid current $\varphi_i(t)$ can be calculated as

$$\varphi_i(t) = \varphi_v(t) + \underbrace{\arcsin\left(\frac{Q_{\rm in,ref}(t)}{S_{\rm in,ref}(t)}\right)}_{\varphi_{PQ}(t)}, \tag{9}$$

where $S^2_{\rm in,ref}(t) = P^2_{\rm in,ref}(t) + Q^2_{\rm in,ref}(t)$ holds,[8] and $\varphi_{PQ}(t)$ is the load angle. The amplitude of the grid current is $I_{g,\rm ref}(t) = S_{\rm in,ref}(t)/V_g$, with $V_g = 1$ p.u. The other reference signals can be calculated by transforming (8) to the dq-reference frame, which rotates with ω_g and its d-axis is aligned with the grid virtual flux $\boldsymbol{\psi}_g$. Subsequently, a phasor analysis is performed, as exemplified in Fig. 5.

B. Objective Function Formulation

Given a prediction horizon of N_p time steps, the aforementioned control objectives are mapped into a scalar by the objective function[9]

$$J(k) = \sum_{\ell=k}^{k+N_p-1} \|\boldsymbol{y}_{\rm ref}(\ell+1) - \boldsymbol{y}(\ell+1)\|^2_{\boldsymbol{Q}} + \lambda_u \|\Delta\boldsymbol{u}(\ell)\|^2_2 . \tag{10}$$

According to (10), the first term is the output tracking error term $\boldsymbol{y}_{\rm err}(\ell+1) = \boldsymbol{y}_{\rm ref}(\ell+1) - \boldsymbol{y}(\ell+1)$, which denotes the deviation of the output variables $\boldsymbol{y}(\ell)$ from their reference values $\boldsymbol{y}_{\rm ref}(\ell)$, calculated as described in Section IV-A. Note that the output error term is weighted with the positive semidefinite matrix $\boldsymbol{Q} \succeq \boldsymbol{0}$ of dimensions 6×6.

Regarding the second term in (10), it denotes the control effort $\Delta\boldsymbol{u}(\ell) = \boldsymbol{u}(\ell) - \boldsymbol{u}(\ell-1)$, and it is introduced to enable smoother control by penalizing the control input changes between consecutive time instants. Moreover, $\lambda_u \in \mathbb{R}^{++}$ is the associated weighting factor. Given that, the optimization variable is the sequence of the three-phase modulating signals over the N_p-step prediction horizon, i.e.,

$$\boldsymbol{U}(k) = \left[\boldsymbol{u}^T(k)\ \boldsymbol{u}^T(k+1)\ \ldots\ \boldsymbol{u}^T(k+N_p-1)\right]^T , \tag{11}$$

the control effort term $\Delta\boldsymbol{u}(\ell)$ is a real-valued vector (rather than an integer as for FCS-MPC), i.e., $\Delta\boldsymbol{u}(\ell) \in \mathbb{R}^3$.

C. Hard and Soft Constraints

Since a modulator is used to translate the modulating signal into switching commands, hard constraints should be imposed on $\boldsymbol{u}(\ell)$. Thus, given the amplitude of the carrier signals, the modulating signal is bounded between -1 and 1 for each prediction horizon time step $\ell = k, k+1, \ldots, k+N_p-1$, i.e.,[10]

$$-\boldsymbol{1}_3 \preceq \boldsymbol{u}(\ell) \preceq \boldsymbol{1}_3 , \tag{12}$$

where $\boldsymbol{1}$ is a vector with all entries equal to one and of dimension as indicated by the subscript. Introducing the matrix $\boldsymbol{V} = [\,\boldsymbol{I}_3\ -\boldsymbol{I}_3\,]^T \in \mathbb{R}^{6\times 3}$, constraint (12) can be written as

$$\boldsymbol{V}\boldsymbol{u}(\ell) \preceq \boldsymbol{1}_6 . \tag{13}$$

As hard constraints on state and/or output variables might cause feasibility issues, we introduce soft constraints on $\boldsymbol{y}(\ell)$ to restrict the operation of the power electronic system within its safe operating area. Such constraints can be formulated as (in)equalities that can be relaxed using slack variables $\xi \in \mathbb{R}^+$. The latter represent the degree of the constraint violation, thus, ξ have to be minimized. For example, the soft constraints on

[8]Note that $P_{\rm in,ref}(t)$ and $Q_{\rm in,ref}(t)$ (as well as $P_{\rm in}(t)$ and $Q_{\rm in}(t)$) commonly refer to the PCC, but here—for the sake of simplicity—refer to the grid voltage source, see Fig. 1(a).

[9]Note that $\|\boldsymbol{\xi}\|^2_{\boldsymbol{Q}} = \boldsymbol{\xi}^T\boldsymbol{Q}\boldsymbol{\xi}$ denotes the squared norm of a vector $\boldsymbol{\xi}$ weighted with the matrix $\boldsymbol{Q}$.

[10]Such hard constraints on the control input imply that operation in overmodulation is possible as saturation of the modulating signal $\boldsymbol{u}_{\rm ref}(k)$ is achieved.

the converter current of phase $x \in \{a, b, c\}$ at time step ℓ are of the form [33]

$$\xi_{\mathrm{conv}}(\ell) \geq i_{\mathrm{conv},x}(\ell) - i_{\mathrm{conv,max}} \tag{14a}$$
$$\xi_{\mathrm{conv}}(\ell) \geq -i_{\mathrm{conv},x}(\ell) - i_{\mathrm{conv,max}} \tag{14b}$$
$$\xi_{\mathrm{conv}}(\ell) \geq 0\,, \tag{14c}$$

where the slack variable ξ_{conv} maps the constraint violation into a nonnegative real number. Note that due to three-phase symmetry, $i_{\mathrm{conv,max}}$ defines both upper and lower bounds, i.e., the trip levels to limit the 3L-NPC switch stress.

For each single-phase component, the three constraints define three lines which restrict the feasible space of the slack variable, indicated by the shaded area in Fig. 6. The slope of the soft constraints relates to the penalty used to weigh $\xi_{\mathrm{conv}}(\ell)$, thus, by heavily penalizing such constraints—effectively—very steep slopes result, see Fig. 6(b). In doing so, the implemented soft constraints can keep $i_{\mathrm{conv},x}(\ell)$ within the desired limits almost as strictly as hard constraints, while guaranteeing that potential numerical or feasibility issues do not arise. Such constraints in vector form can be written as

$$\mathbf{1}_7 \xi_{\mathrm{conv}}(\ell) \succeq \boldsymbol{W}\boldsymbol{K}^{-1}\boldsymbol{i}_{\mathrm{conv}}(\ell) - \begin{bmatrix} \mathbf{1}_6 \\ 0 \end{bmatrix} i_{\mathrm{conv,max}}\,, \tag{15}$$

with $\boldsymbol{K}^{-1}$ being the pseudoinverse of the (reduced) Clarke transformation matrix $\boldsymbol{K}$, and

$$\boldsymbol{W} = \begin{bmatrix} 1 & -1 & 0 & 0 & 0 & 0 & 0 \\ 0 & 0 & 1 & -1 & 0 & 0 & 0 \\ 0 & 0 & 0 & 0 & 1 & -1 & 0 \end{bmatrix}^T .$$

Similar to (15), upper and lower constraints are imposed on the capacitor voltage, with $v_{c,\max}$ referring to ξ_c, and on the grid current, with $i_{g,\max}$ to ξ_g. By aggregating the slack variables in the vector

$$\boldsymbol{\xi}(\ell) = [\xi_{\mathrm{conv}}(\ell)\ \xi_c(\ell)\ \xi_g(\ell)]^T \in \mathbb{R}^3\,, \tag{16}$$

the soft constraints on all variables of interest are written as

$$\boldsymbol{M}\boldsymbol{\xi}(\ell) \succeq \widetilde{\boldsymbol{W}}\widetilde{\boldsymbol{K}}\boldsymbol{C}\boldsymbol{x}(\ell) - \boldsymbol{N}\boldsymbol{c}\,, \tag{17}$$

where $\boldsymbol{c} = [i_{\mathrm{conv,max}}\ v_{c,\max}\ i_{g,\max}]^T$ and

$$\boldsymbol{M} = \begin{bmatrix} \mathbf{1}_7 & \mathbf{0}_7 & \mathbf{0}_7 \\ \mathbf{0}_7 & \mathbf{1}_7 & \mathbf{0}_7 \\ \mathbf{0}_7 & \mathbf{0}_7 & \mathbf{1}_7 \end{bmatrix}, \quad \boldsymbol{N} = \begin{bmatrix} \mathbf{1}_6 & 0 & \mathbf{0}_6 & 0 & \mathbf{0}_6 & 0 \\ \mathbf{0}_6 & 0 & \mathbf{1}_6 & 0 & \mathbf{0}_6 & 0 \\ \mathbf{0}_6 & 0 & \mathbf{0}_6 & 0 & \mathbf{1}_6 & 0 \end{bmatrix}^T ,$$
$$\widetilde{\boldsymbol{W}} = \mathrm{diag}\,(\boldsymbol{W}, \boldsymbol{W}, \boldsymbol{W})\,, \quad \widetilde{\boldsymbol{K}} = \mathrm{diag}\left(\boldsymbol{K}^{-1}, \boldsymbol{K}^{-1}, \boldsymbol{K}^{-1}\right).$$

D. Optimization Problem

To minimize the slack variables, i.e., to avoid as much violation of the (soft) output constraints as possible, the term

$$\sum_{\ell=k}^{k+N_p-1} \|\boldsymbol{\xi}(\ell+1)\|^2_{\boldsymbol{R}} \tag{18}$$

is added to (10) and weighted with the penalty matrix $\boldsymbol{R} \succeq \mathbf{0}$ of dimensions 3×3. Thus the objective function becomes

$$J(k) = \sum_{\ell=k}^{k+N_p-1} \|\boldsymbol{y}_{\mathrm{err}}(\ell+1)\|^2_{\boldsymbol{Q}} + \lambda_u \|\Delta\boldsymbol{u}(\ell)\|_2^2 + \|\boldsymbol{\xi}(\ell+1)\|^2_{\boldsymbol{R}}\,. \tag{19}$$

In (19), the weighting matrices $\boldsymbol{Q}$, $\boldsymbol{R}$, and the weighting factor λ_u prioritize among the conflicting goals of the controller. Large positive values are chosen for $\boldsymbol{R}$ to heavily penalize the slack variables in $J(k)$ so as to achieve a behavior as close to that with hard constraints as possible. In doing so, violations of the protection constraints are minimal, if not avoided altogether. As a result, significant component stresses and unexpected system interruptions are prevented, which, in turn, enhances the reliability and life-time of the system.

By introducing the sequence of slack variables over the prediction horizon as

$$\boldsymbol{\Xi}(k) = \left[\boldsymbol{\xi}^T(k+1)\ \boldsymbol{\xi}^T(k+2)\ \ldots\ \boldsymbol{\xi}^T(k+N_p)\right]^T \tag{20}$$

the optimization variable becomes

$$\widetilde{\boldsymbol{U}}(k) = \left[\boldsymbol{U}^T(k)\ \boldsymbol{\Xi}^T(k)\right]^T . \tag{21}$$

As there are three manipulated variables and three slack variables at each time step, the optimization vector is of the dimension $6N_p$, thus, $\widetilde{\boldsymbol{U}}(k) \in \mathbb{R}^{6N_p}$. Based on the above, the optimization problem takes the form

$$\underset{\widetilde{\boldsymbol{U}}(k)\,\in\,\mathbb{R}^{6N_p}}{\text{minimize}} \quad J(k) \tag{22a}$$
$$\text{subject to} \quad \boldsymbol{x}(\ell+1) = \boldsymbol{A}\boldsymbol{x}(\ell) + \boldsymbol{B}\boldsymbol{u}(\ell) \tag{22b}$$
$$\boldsymbol{y}(\ell+1) = \boldsymbol{C}\boldsymbol{x}(\ell+1) \tag{22c}$$
$$\Delta\boldsymbol{u}(\ell) = \boldsymbol{u}(\ell) - \boldsymbol{u}(\ell-1) \tag{22d}$$
$$\widetilde{\boldsymbol{W}}\widetilde{\boldsymbol{K}}\boldsymbol{C}\boldsymbol{x}(\ell+1) - \boldsymbol{M}\boldsymbol{\xi}(\ell+1) \preceq \boldsymbol{N}\boldsymbol{c} \tag{22e}$$
$$\boldsymbol{V}\boldsymbol{u}(\ell) \preceq \mathbf{1}_6 \tag{22f}$$
$$\forall \ell = k, \ldots, k+N_p-1\,.$$

As function (19) is quadratic and subjected to the evolution of a linear state-space model with linear inequality constraints, the resulting optimization problem is a QP. In particular, (22) is a strictly convex QP since the Hessian matrix is positive definite [34], as explained in Section IV-E. Note that since V_{dc} is time invariant the optimization problem is time invariant as well. The QP can be solved efficiently on embedded hardware by using off-the-shelf solvers, e.g., [27]–[29].

The result of the optimization stage is the sequence of optimal manipulated variables $\widetilde{\boldsymbol{U}}^*(k)$ at time step k, i.e.,

$$\widetilde{\boldsymbol{U}}^*(k) = \left[\widetilde{\boldsymbol{u}}^{*T}(k)\ \widetilde{\boldsymbol{u}}^{*T}(k+1)\ \ldots\ \widetilde{\boldsymbol{u}}^{*T}(k+N_p-1)\right]^T . \tag{23}$$

Out of this sequence the first element $\widetilde{\boldsymbol{u}}^*(k)$ is selected, while the rest are discarded in line with the receding horizon control principle [35]. Note that from $\widetilde{\boldsymbol{u}}^*(k)$ the three first entries—corresponding to $\boldsymbol{u}^*(k)$, i.e., the optimal modulating signal at step k—are extracted and fed into the 3L CB-PWM stage.

E. Optimization Problem in Vector Form

To write the QP in a form suitable for embedded implementation, the optimization problem has to be rewritten in a vector form. According to [36], a condensed QP formulation is preferable and typically computationally favorable when the size of the optimization problem is relatively small, as is the case with (22).

Considering the output reference vector over the horizon N_p

$$\boldsymbol{Y}_{\mathrm{ref}}(k) = \left[\boldsymbol{y}_{\mathrm{ref}}^T(k+1)\ \boldsymbol{y}_{\mathrm{ref}}^T(k+2)\ \ldots\ \boldsymbol{y}_{\mathrm{ref}}^T(k+N_p)\right]^T, \tag{24}$$

and after some algebraic manipulations, function (19) can be written in a vector form as

$$\begin{aligned} J(k) = &\left\|\boldsymbol{Y}_{\mathrm{ref}}(k) - \boldsymbol{\Gamma}\boldsymbol{x}(k) - \boldsymbol{\Upsilon}\boldsymbol{U}(k)\right\|_{\widetilde{\boldsymbol{Q}}}^2 \\ &+ \lambda_u \left\|\boldsymbol{S}\boldsymbol{U}(k) - \boldsymbol{E}\boldsymbol{u}(k-1)\right\|_2^2 + \left\|\boldsymbol{\Xi}(k)\right\|_{\widetilde{\boldsymbol{R}}}^2 , \end{aligned} \tag{25}$$

where $\widetilde{\boldsymbol{Q}} = \mathrm{diag}\,(\boldsymbol{Q},\ldots,\boldsymbol{Q})$ and $\widetilde{\boldsymbol{R}} = \mathrm{diag}\,(\boldsymbol{R},\ldots,\boldsymbol{R})$, with dimensions $6N_p \times 6N_p$ and $3N_p \times 3N_p$, respectively, while matrices $\boldsymbol{\Gamma}$, $\boldsymbol{\Upsilon}$, $\boldsymbol{S}$, and $\boldsymbol{E}$ are given in the appendix. By introducing the auxiliary matrices and variable

$$\begin{aligned} \boldsymbol{H} &= \boldsymbol{\Upsilon}^T\widetilde{\boldsymbol{Q}}\boldsymbol{\Upsilon} + \lambda_u \boldsymbol{S}^T\boldsymbol{S} \\ \boldsymbol{\Theta}(k) &= -\boldsymbol{\Upsilon}^T\widetilde{\boldsymbol{Q}}\left(\boldsymbol{Y}_{\mathrm{ref}}(k) - \boldsymbol{\Gamma}\boldsymbol{x}(k)\right) - \lambda_u \boldsymbol{S}^T\boldsymbol{E}\boldsymbol{u}(k-1) \\ \theta(k) &= \left\|\boldsymbol{Y}_{\mathrm{ref}}(k) - \boldsymbol{\Gamma}\boldsymbol{x}(k)\right\|_{\widetilde{\boldsymbol{Q}}}^2 + \lambda_u \left\|\boldsymbol{E}\boldsymbol{u}(k-1)\right\|_2^2 , \end{aligned}$$

function (25) is rewritten as[11]

$$\begin{aligned} J(k) &= \boldsymbol{U}^T(k)\boldsymbol{H}\boldsymbol{U}(k) + \boldsymbol{\Xi}^T(k)\widetilde{\boldsymbol{R}}\boldsymbol{\Xi}(k) + 2\boldsymbol{\Theta}^T(k)\boldsymbol{U}(k) \\ &= \widetilde{\boldsymbol{U}}^T(k)\widetilde{\boldsymbol{H}}\widetilde{\boldsymbol{U}}(k) + 2\boldsymbol{d}^T(k)\widetilde{\boldsymbol{U}}(k) , \end{aligned} \tag{27}$$

where the Hessian matrix $\widetilde{\boldsymbol{H}} \succ 0$ is the block diagonal matrix $\widetilde{\boldsymbol{H}} = \mathrm{diag}(\boldsymbol{H}, \widetilde{\boldsymbol{R}})$ and $\boldsymbol{d}(k) = [\boldsymbol{\Theta}^T(k)\ \boldsymbol{0}_{3N_p}^T]^T$.

The input constraints in (22) in vector form are

$$\begin{aligned} \boldsymbol{\Omega}\boldsymbol{U}(k) &\preceq \boldsymbol{1}_{6N_p} \Leftrightarrow \\ \left[\boldsymbol{\Omega}\ \boldsymbol{0}_{6N_p\times 3N_p}\right]\widetilde{\boldsymbol{U}}(k) &\preceq \boldsymbol{1}_{6N_p} , \end{aligned} \tag{28}$$

where $\boldsymbol{\Omega} = \mathrm{diag}\,(\boldsymbol{V},\ldots,\boldsymbol{V})$ of dimension $6N_p \times 3N_p$, while the output constraints can be written as

$$\begin{aligned} \boldsymbol{Z}\boldsymbol{\Xi}(k) &\preceq \boldsymbol{\Delta} - \boldsymbol{\Pi}\left(\boldsymbol{\Gamma}\boldsymbol{x}(k) + \boldsymbol{\Upsilon}\boldsymbol{U}(k)\right) \Leftrightarrow \\ \boldsymbol{Z}\boldsymbol{\Xi}(k) + \boldsymbol{\Pi}\boldsymbol{\Upsilon}\boldsymbol{U}(k) &\preceq \boldsymbol{\Delta} - \boldsymbol{\Pi}\boldsymbol{\Gamma}\boldsymbol{x}(k) \Leftrightarrow \\ \left[\boldsymbol{\Pi}\boldsymbol{\Upsilon}\ \boldsymbol{Z}\right]\widetilde{\boldsymbol{U}}(k) &\preceq \boldsymbol{\Delta} - \boldsymbol{\Pi}\boldsymbol{\Gamma}\boldsymbol{x}(k) , \end{aligned} \tag{29}$$

where the matrices $\boldsymbol{Z}$, $\boldsymbol{\Pi}$, and $\boldsymbol{\Delta}$ are defined as

$$\begin{aligned} \boldsymbol{Z} &= \mathrm{diag}\,(-\boldsymbol{M},\ldots,-\boldsymbol{M}) , \\ \boldsymbol{\Pi} &= \mathrm{diag}\left(\widetilde{\boldsymbol{W}}\widetilde{\boldsymbol{K}},\ldots,\widetilde{\boldsymbol{W}}\widetilde{\boldsymbol{K}}\right) , \\ \boldsymbol{\Delta} &= \left[(\boldsymbol{N}\boldsymbol{c})^T\ \ldots\ (\boldsymbol{N}\boldsymbol{c})^T\right]^T , \end{aligned}$$

with dimensions $21N_p \times 3N_p$, $21N_p \times 6N_p$, and $21N_p \times 1$, respectively.

By combining (28) and (29) into one expression, the optimization problem (22) takes its final form suitable for embedded implementation, i.e.,

$$\begin{aligned} &\underset{\widetilde{\boldsymbol{U}}(k)\,\in\,\mathbb{R}^{6N_p}}{\text{minimize}}\ \ \widetilde{\boldsymbol{U}}^T(k)\widetilde{\boldsymbol{H}}\widetilde{\boldsymbol{U}}(k) + 2\boldsymbol{d}^T(k)\widetilde{\boldsymbol{U}}(k) \\ &\text{subject to}\ \ \begin{bmatrix}\boldsymbol{\Omega} & \boldsymbol{0}_{6N_p\times 3N_p} \\ \boldsymbol{\Pi}\boldsymbol{\Upsilon} & \boldsymbol{Z}\end{bmatrix}\widetilde{\boldsymbol{U}}(k) \preceq \begin{bmatrix}\boldsymbol{1}_{6N_p} \\ \boldsymbol{\Delta} - \boldsymbol{\Pi}\boldsymbol{\Gamma}\boldsymbol{x}(k)\end{bmatrix}. \end{aligned} \tag{31}$$

As shown in Section VII-B, the condensed QP (31) facilitates and speeds up the real-time implementation of the proposed MPC algorithm.

[11]Note that in (27), the term $\theta(k)$ is omitted since it merely adds an offset to the total cost, i.e., $J(k) = \boldsymbol{U}^T(k)\boldsymbol{H}\boldsymbol{U}(k) + \boldsymbol{\Xi}^T(k)\widetilde{\boldsymbol{R}}\boldsymbol{\Xi}(k) + 2\boldsymbol{\Theta}^T(k)\boldsymbol{U}(k) + \theta(k)$.

TABLE I
MV SYSTEM RATED VALUES AND PARAMETERS

rated voltage V_R	3.3 kV	filter inductance L_{fg}	0.403 mH
rated current I_R	1575 A	filter resistance R_{fg}	0.484 mΩ
apparent power S_R	9 MVA	filter inductance L_{fc}	0.452 mH
grid frequency f_g	50 Hz	filter resistance R_{fc}	0.484 mΩ
dc-link voltage V_{dc}	5.4 kV	filter capacitance C	884.9 μF
dc capacitor C_{dc}	15 mF	filter resistance R_c	0.484 mΩ
grid inductance L_g	0.192 mH	leakage inductance L_t	0.385 mH
grid resistance R_g	6.019 mΩ	leakage resistance R_t	10.10 mΩ

V. Simulation Results

The performance of the proposed indirect MPC scheme is evaluated at steady-state operating conditions and during transients through MATLAB simulations. The QP is solved with the `quadprog` solver that employs an active-set (AS) method. The system rated values and parameters are given in Table I. The MPC scheme is executed at the (upper and lower) peaks of the triangular carrier, with $f_c = 750$ Hz, implying a sampling interval of $T_s = 1/(2f_c) = 666.67\,\mu$s. According to Table I, the dominant resonance frequency is $f_{\mathrm{res}} = 304$ Hz. The prediction horizon is $N_p = 4$. Shorter horizons might adversely affect the closed-loop system stability (as also discussed in Section VI), hence, a relatively long prediction horizon—combined with the full-state information of MPC—can render an additional active damping loop unnecessary [15], [37]. Note that the full state $\boldsymbol{x}$ is measured and assumed to be available to the controller along with $\boldsymbol{y}_{\mathrm{ref}}$. Moreover, the implemented control action is fed into the modulator and kept constant between time steps k and $k+1$. Regarding the modulator, asymmetric regularly sampled 3L CB-PWM with PD is used. Finally, all results are presented in the p.u. system.

A. Choice of the Design Parameters

The main goal of the tuning procedure is to prioritize the grid current reference tracking to reduce the grid current TDD, $I_{g,\mathrm{TDD}}$, while minimizing the violation of the soft constraints. Hence, the error $\boldsymbol{i}_{g,\mathrm{ref}}(\ell+1) - \boldsymbol{i}_g(\ell+1)$ is prioritized over the error of the other controlled variables by assigning bigger values to the associated entries of $\boldsymbol{Q}$. Moreover, the tracking of $\boldsymbol{i}_{\mathrm{conv,ref}}$ is prioritized over that of $\boldsymbol{v}_{c,\mathrm{ref}}$ to avoid an (indirect) deterioration in the tracking performance of the grid current. Given these, the weighting matrix of the output error term is chosen as $\boldsymbol{Q} = \mathrm{diag}\,(10,10,1,1,100,100)$. Furthermore, the weighting factor on the manipulated variable is chosen as $\lambda_u = 1$ to prevent aggressive control actions during transients. As for the soft constraints, these are activated at $i_{\mathrm{conv,max}} = 1.3$ p.u., $v_{c,\mathrm{max}} = 1.25$ p.u., and $i_{g,\mathrm{max}} = 1.25$ p.u. To ensure that the latter are not violated during transients, high values are assigned to the nonzero entries of $\boldsymbol{R}$, i.e., $\boldsymbol{R} = \mathrm{diag}\left(10^5, 10^5, 1\right)$. Note that since the grid current tracking is prioritized with $\boldsymbol{Q}$, big deviations—and thus overcurrents—of the grid current are already penalized, thus, a high penalty on ξ_g is redundant.

B. Steady-State Operation

The steady-state performance of the proposed indirect MPC is shown in Fig. 7. More specifically, Fig. 7(a) shows the

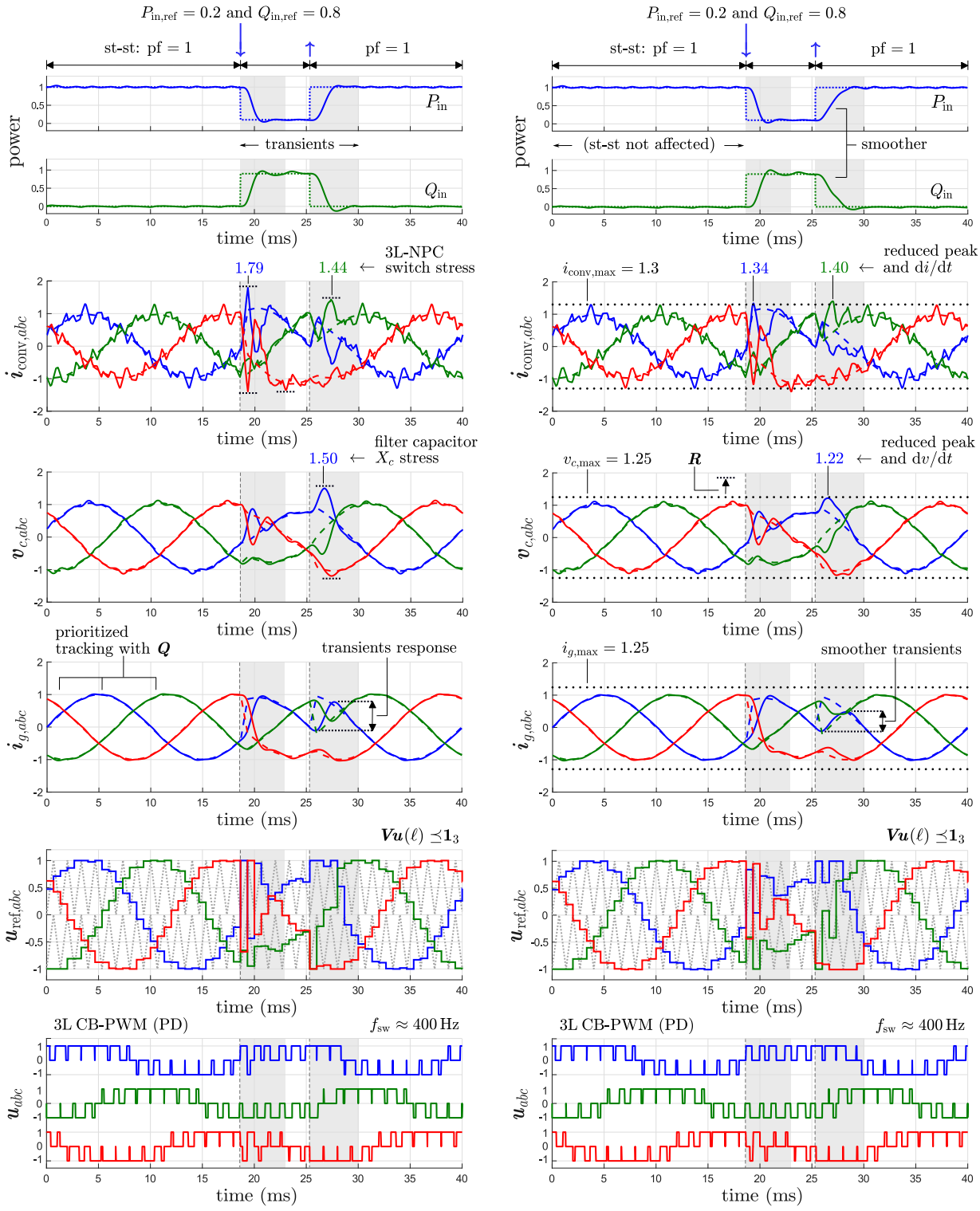

(a) (b)

Fig. 7. Simulated waveforms produced by indirect MPC with $N_p = 4$, when the soft constraints are (a) not included, and (b) included. The results are shown over two fundamental periods $2T_g$, with $T_g = 1/f_g = 20$ ms. Both steady-state and transient operations are tested. From top to bottom: real power P_{in} (blue line) and reactive power Q_{in} (green line) and their references (dashed lines); three-phase converter input currents $\boldsymbol{i}_{\text{conv},abc}$ (with phase a, b and c denoted as blue, red and green lines, respectively) and the related references; three-phase capacitor voltage $\boldsymbol{v}_{c,abc}$; three-phase grid currents $\boldsymbol{i}_{g,abc}$; three-phase modulating signal $\boldsymbol{u}_{abc,\text{ref}}$ along with the two carrier waveforms (gray dotted lines); three-phase switch positions $\boldsymbol{u}_{abc}$.

system behavior when the soft constraints are not included in the MPC problem, whereas Fig. 7(b) depicts the system response when the aforementioned constraints are taken into account. In both cases, operation at nominal active power and zero reactive power is considered, i.e., $P_{\text{in,ref}} = 1$ and $Q_{\text{in,ref}} = 0$ with pf $= 1$. As can be seen in Fig. 7, all output variables $\boldsymbol{y}_{abc}$ accurately track their reference values. Hence, they are effectively sinusoidal, despite operation at a low switching frequency of $f_{\text{sw}} = 400$ Hz. Note that the latter is close to the resonance frequency f_{res}. It is worth mentioning

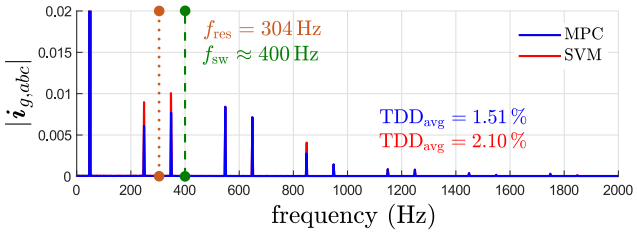

(a)

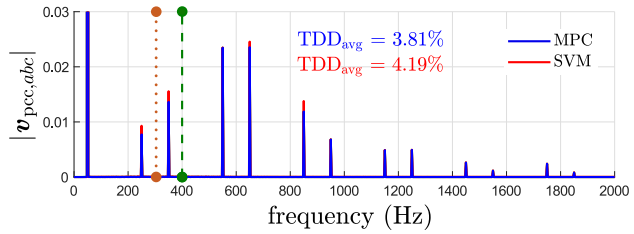

(b)

Fig. 8. Harmonic spectra of the (a) grid current, and (b) PCC voltage. For both cases, the harmonics do not violate their respective limits imposed by the IEEE 519 and IEC 61000-2-4 standards, respectively.

that the soft constraints (shown as black dotted lines in Fig. 7(b)) are not activated during steady-state operation, hence the MPC algorithm performs the same, whether there are soft constraints or not. On the other hand, the constraints on the control input, i.e., the three-phase modulating signal $\boldsymbol{u}_{abc,\text{ref}}$, are activated and fully respected since they are implemented as hard constraints. In doing so, the instantaneous values of the modulating signal are always less than the peak values of the triangular carrier and the comparisons in line with the CB-PWM principle can be successfully performed. Hence, by driving this signal to the subsequent modulation stage, the three-phase switch positions—which are applied to the converter—are generated, see the last row of figures in Fig. 7.

To assess if the grid current and PCC voltage produced by the proposed MPC algorithm meet the grid standards, the relevant harmonic spectra are examined. To this aim, Fig. 8(a) shows the harmonic spectrum of the grid current $\boldsymbol{i}_{g,abc}$. As mentioned above, it can be observed that despite the very low switching frequency—which is very close to the resonance frequency—the grid current distortions are very low, resulting in a TDD value of $I_{g,\text{TDD}} = 1.51\%$. Moreover, the harmonics are at odd, non-triplen multiplies of the fundamental frequency, with sidebands around the carrier frequency. Given that $k_{\text{sc}} \approx 19.96$, the IEEE 519 standard indicates a maximum $I_{g,\text{TDD,max}} = 5\%$ with the tighter limits imposed above the 35^{th} harmonic. Thus, the stringent limits on the grid current harmonics are adhered to. Likewise, Fig. 8(b) shows the spectrum of the voltage at the PCC along with its (low) TDD value. Given the limitations imposed by the IEC 61000-2-4 for a Class 2 electromagnetic environment, it can be concluded that they are fully respected.

Based on the above results, it can be claimed that the proposed controller can produce grid currents with low distortions (i.e., low $I_{g,\text{TDD}}$) and without exciting the resonance frequency f_{res}. This outcome is achieved without the existence of an additional damping loop, which highlights the simpler structure of the discussed MIMO MPC scheme.

Finally, as a benchmark, convectional CB-PWM with a suitable common-mode signal injection is used such that equivalence with SVM is achieved [17]. Moreover, for a fair comparison, operation at the same f_{sw} is considered. This can be interpreted as having a simple closed-loop linear controller with a very low bandwidth. As can be seen in Fig. 8(a), the grid current harmonics produced by SVM are of the same order, but slightly different amplitude, compared with those of indirect MPC. As a result, the grid current TDD with SVM is slightly higher ($I_{g,\text{TDD}} = 2.10\%$) than that of MPC. The same trend is observed in the harmonic spectrum of the voltage at the PCC, see Fig. 8(b); as with the grid current, the voltage harmonics are similar, but of slightly higher amplitude, giving rise to a voltage TDD of 4.19%.

C. Transient Operation

To investigate the dynamic behavior of the closed-loop system, input power reference steps are applied. At $t = 18\,\text{ms}$, $P_{\text{in,ref}}$ is changed from 1 to $0.2\,\text{p.u.}$ and back to $1\,\text{p.u.}$ at $t = 26\,\text{ms}$. Likewise, $Q_{\text{in,ref}}$ is changed from 0 to $0.8\,\text{p.u.}$ and back to $0\,\text{p.u.}$ at the same time instants. These transients are indicating a high stress in the grid due to a large load demand. As can be seen in both Figs. 7(a) and 7(b), the controlled variables—and consequently the powers—accurately follow their references.

The ability of the proposed MPC algorithm to respect operational constraints on the output variables can be appreciated by comparing Fig. 7(a) (i.e., MPC without soft constraints) with Fig. 7(b) (i.e., MPC with soft constraints). As can be seen, in the former figure, the variables $\boldsymbol{i}_{\text{conv},abc}$ and $\boldsymbol{v}_{c,abc}$ exhibit significant overshoots during transients, violating the associated trip levels. For instance, peak values $i_{\text{conv},a} = 1.79\,\text{p.u.}$ and $i_{\text{conv},c} = 1.44\,\text{p.u.}$ are 49% and 14% above $i_{\text{conv,max}} = 1.3\,\text{p.u.}$, respectively, while the trip levels violations occur over an interval of $330\,\mu\text{s}$ for phase a and $540\,\mu\text{s}$ for phase c. As discussed in Section II-B, such current excursions may damage the hardware, thus they should be avoided. Similar considerations apply to the capacitor voltage, which presents a peak of $v_{c,a} = 1.50\,\text{p.u.}$, and an overvoltage time interval of $990\,\mu\text{s}$ given that $v_{c,\text{max}} = 1.25\,\text{p.u.}$ Such conditions may have a strong impact on the capacitor electro-thermal stresses. To avoid this, X_c is often oversized, leading to a bigger filter and thus an increased cost of the system.

On the other hand, when the MPC problem (31) is implemented, the soft constraints on the output variables are activated, see Fig. 7(b). As can be observed, due to the heavy penalization of the associated slack variables, all controlled variables remain mostly within their bounds, with minute violations occurring in the converter current. Notwithstanding the foregoing, overcurrents and/or overvoltages are prevented, thus the hardware of the system is protected from potential damages and/or trips. It is worth mentioning, however, that when the soft constraints are included in the optimization problem the controller is less aggressive since it tries to keep the controlled variables within their safety limits. As a result, the settling time of the power transient during the step-down change in $P_{\text{in,ref}}$ is about $2\,\text{ms}$ when the constraints

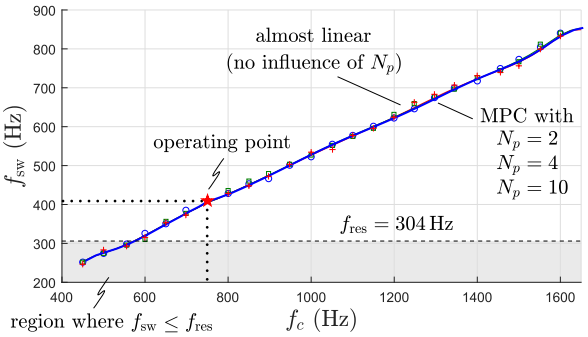

(a)

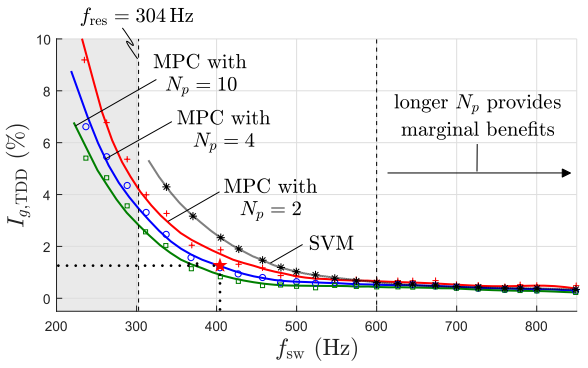

(b)

Fig. 9. Trade-off curves between (a) the device switching frequency $f_{\rm sw}$ and the carrier frequency f_c, and (b) the grid current TDD $I_{g,\rm TDD}$ and $f_{\rm sw}$, for the proposed indirect MPC algorithm with different horizons ($N_p = 2, 4, 10$). In (b) the current TDD with vector control and SVM is also shown.

are not taken into account, as opposed to 2.2 ms, which is the time required from the constrained MPC. As for the step-up change in $P_{\rm in,ref}$, the unconstrained MPC requires 3 ms to settle to the new operating point, i.e., longer than before due to the limited available voltage margin, whereas the transient time with the constrained MPC is 3.98 ms. Both methods, however, try to eliminate the output tracking error as quickly as possible. This is evident from the computed control input (i.e., modulating signal) which is saturated at the corresponding maximal/minimal allowable values, see the second-to-bottom row of figures in Figs. 7(a) and 7(b).

VI. Sensitivity of the Closed-Loop Performance

In this section, the impact of the prediction horizon and carrier frequency on the closed-loop performance of the proposed MPC algorithm are investigated, both at steady-state operation and during transients. Moreover, since the choice of weighting factors affects the controller behavior as well as the conditioning of the QP problem (31) [36], the sensitivity of the closed-loop performance to variations in the matrix $\boldsymbol{R}$ is analyzed to provide a deeper insight in the controller design.

A. Variations in the Carrier Frequency and Horizon Length

Simulation results obtained at rated power are used to analyze the steady-state and dynamic behavior of the controller. The former is examined under variations in the carrier frequency f_c and the length of the prediction horizon N_p. To this end, the device switching frequency $f_{\rm sw}$ and the grid current TDD $I_{g,\rm TDD}$ are used as performance metrics. Moreover, the impact of the prediction horizon length on the transient performance of the controller—as quantified by the peak values of the single-phase converter current $i_{{\rm conv},a({\rm pk})}$ and filter capacitor voltage $v_{c,a({\rm pk})}$—is also investigated.

1) Steady-State Operation: In a first test, the carrier frequency of the multilevel PWM is varied between 450 and 1650 Hz with a step of 50 Hz. The resulting device switching frequency $f_{\rm sw}$ is illustrated in Fig. 9(a) for different lengths of the prediction horizon. As expected, the horizon steps N_p do not affect the switching frequency since this is dictated by the carrier frequency.

For the range of achieved $f_{\rm sw}$, Fig. 9(b) shows the grid current TDD $I_{g,\rm TDD}$. As can be seen, $I_{g,\rm TDD}$ increases as $f_{\rm sw}$ decreases. It is worth mentioning, however, that MPC can successfully control the system even at very low switching frequencies and still produce very low current TDD. This is indeed a promising result, because it shows that the proposed MPC scheme can be used in applications that require very low device switching frequencies, which are as close to the resonance frequency $f_{\rm res}$ as possible. Moreover, as can be observed, the length of the horizon has a positive effect on $I_{g,\rm TDD}$, since the latter decreases as N_p increases. This is even more pronounced at low switching frequencies, and close to (or lower than) the resonance frequency, where the active damping attribute of the controller becomes more evident. For comparison purposes, the current TDD produced by vector control with SVM and without active damping is depicted. It is clear, that the current TDD of SVM is greater than that of MPC over a wide range of switching frequencies. This difference becomes more apparent at switching frequencies close to the resonance. Finally, it is noteworthy that due to lack of (passive or active) damping, vector control with SVM fails to control the system for $f_{\rm sw}$ close to $f_{\rm res}$, where closed-loop stability is lost.

For the second test, the carrier frequency is kept constant at $f_{\rm c} = 750\,{\rm Hz}$ (i.e., $f_{\rm sw} = 400\,{\rm Hz}$) while N_p is varied between 1 and 10, see Table II. Recall that, as shown in Fig. 9(a), the prediction horizon length does not affect the device switching frequency $f_{\rm sw}$. However, N_p has an impact on the grid current TDD, as also indicated in Fig. 9(b). As can be seen in the second column of Table II, a one-step horizon can give rise to closed-loop stability issues. This is due to the presence of the slow capacitor voltage dynamics and the undamped resonance, since both require a sufficiently long prediction horizon to be successfully tackled. On the other hand, as the horizon increases stability is ensured and the quality of the grid current improves. This finding is in line with the existing literature [15], [25]. It is noteworthy, nevertheless, that for $N_p > 4$ the improvement in terms of $I_{g,\rm TDD}$ is minute, which motivates the use of a four-step horizon to keep the size of the QP (31) relatively small, and thus the associated computational complexity modest.

2) Transient Operation: To gain insight into the impact of N_p on the transient performance, MPC with and without the soft constraints is examined. To this aim, the same power transients as those in Fig. 7 are considered with $\boldsymbol{Q} = {\rm diag}(10, 10, 1, 1, 100, 100)$, $\boldsymbol{R} = {\rm diag}(10^5, 10^5, 1)$, and

TABLE II

INFLUENCE OF THE PREDICTION HORIZON N_p ON (A) THE GRID CURRENT TDD $I_{g,\mathrm{TDD}}$ DURING STEADY-STATE OPERATION, AND (B) THE PEAK VALUES OF THE SINGLE-PHASE CONVERTER CURRENT $i_{\mathrm{conv},a(\mathrm{pk})}$ AND FILTER CAPACITOR VOLTAGE $v_{c,a(\mathrm{pk})}$ DURING TRANSIENTS WITH AND WITHOUT THE SOFT CONSTRAINTS. THE CARRIER FREQUENCY IS $f_c = 750\,\mathrm{Hz}$, $\boldsymbol{Q} = \mathrm{diag}(10, 10, 1, 1, 100, 100)$, AND $\boldsymbol{R} = \mathrm{diag}(10^5, 10^5, 1)$.

N_p (steps)	steady-state		transient			
			indirect MPC without soft constraints		indirect MPC with soft constraints	
	$I_{g,\mathrm{TDD}}$ (%)	$V_{\mathrm{pcc,TDD}}$ (%)	$i_{\mathrm{conv},a(\mathrm{pk})}$ (p.u.)	$v_{c,a(\mathrm{pk})}$ (p.u.)	$i_{\mathrm{conv},a(\mathrm{pk})}$ (p.u.)	$v_{c,a(\mathrm{pk})}$ (p.u.)
1	unstable		unstable		unstable	
2	1.659	4.076	1.954 (+65.4%)	1.541 (+29.1%)	1.342 (+4.2%)	1.252 (+0.2%)
3	1.553	3.861	1.846 (+54.6%)	1.528 (+27.8%)	1.339 (+3.9%)	1.239 (−1.1%)
4	1.507	3.809	1.785 (+48.5%)	1.497 (+24.7%)	1.338 (+3.8%)	1.221 (−2.9%)
5	1.502	3.797	1.782 (+48.2%)	1.491 (+24.1%)	1.338 (+3.8%)	1.221 (−2.9%)
7	1.499	3.791	1.776 (+47.6%)	1.483 (+23.3%)	1.337 (+3.7%)	1.219 (−3.1%)
10	1.487	3.785	1.776 (+47.6%)	1.483 (+23.3%)	1.337 (+3.7%)	1.219 (−3.1%)

*percentages are computed according to $i_{\mathrm{conv,max}} = 1.3\,\mathrm{pu}$ and $v_{c,\mathrm{max}} = 1.25\,\mathrm{pu}$

$f_{\mathrm{sw}} = 750\,\mathrm{Hz}$. The relevant performance metrics, namely $i_{\mathrm{conv},a(\mathrm{pk})}$ and $v_{c,a(\mathrm{pk})}$, are shown in Table II.

As can be seen in Table II, $N_p = 2$ leads to a current peak $i_{\mathrm{conv},a(\mathrm{pk})} \approx 1.95\,\mathrm{p.u.}$ (i.e., $+65.4\%$ above $i_{\mathrm{conv,max}} = 1.3\,\mathrm{p.u.}$) when soft constraints are not imposed on the output variables. This is greater than the peak of $1.79\,\mathrm{p.u.}$ $(+48.5\%)$ obtained with $N_p = 4$ (see also Fig. 7(a)). Moreover, as the horizon is extended, the current peaks are further reduced. Same observations apply to the peak values of the capacitor voltage. Hence, it can be deduced that a longer horizon manages to improve the transient performance of MPC since it can attenuate the overcurrents and overvoltages. This is thanks to the fact that MPC can predict the behavior of the plant for a longer interval in the future, and thus make such control decisions that aim for smooth and accurate tracking of the output reference values, i.e., control actions that indirectly mitigate the spikes in the controlled variables.

When the output variables are constrained such that the system hardware is protected, it is evident that the system is operated within its safe operating area, see Table II. For example, when considering the slack variables $\boldsymbol{\xi}(\ell)$, the current peak is largely attenuated even for $N_p = 2$, where $i_{\mathrm{conv},a(\mathrm{pk})} \approx 1.34\,\mathrm{p.u.}$ (i.e., $+4.2\%$ greater than $i_{\mathrm{conv,max}}$), which is clearly less than the $+65.4\%$ violation occurring without $\boldsymbol{\xi}(\ell)$. Moreover, as with the unconstrained case, an increasing horizon positively affects the dynamic behavior of the controller. However, it can be observed that the improvement is marginal for $N_p > 4$, which—as with the steady-state performance—indicates that $N_p = 4$ suffices to achieve superior performance for the examined system.

B. Variations in the Weighting Factors

As already mentioned in Section V-A, the tuning of the weighting factors $\boldsymbol{Q}$, $\boldsymbol{R}$, and λ_u affects the controller behavior. Considering that the entries of $\boldsymbol{Q}$ are chosen such that the grid current reference tracking is prioritized [25], the choice of $\boldsymbol{R}$ is worth investigating since it influences the dynamic performance of the proposed MPC algorithm.

For the results presented thus far, $\boldsymbol{R}$ is chosen as $\boldsymbol{R} = \mathrm{diag}(10^5, 10^5, 1)$ to avoid potential violation of $i_{\mathrm{conv,max}}$ and $v_{c,\mathrm{max}}$. To provide a deeper analysis of the effect of $\boldsymbol{R}$ on the violation of the soft constraints and the transient responses of the controller that will help understand the controller design,

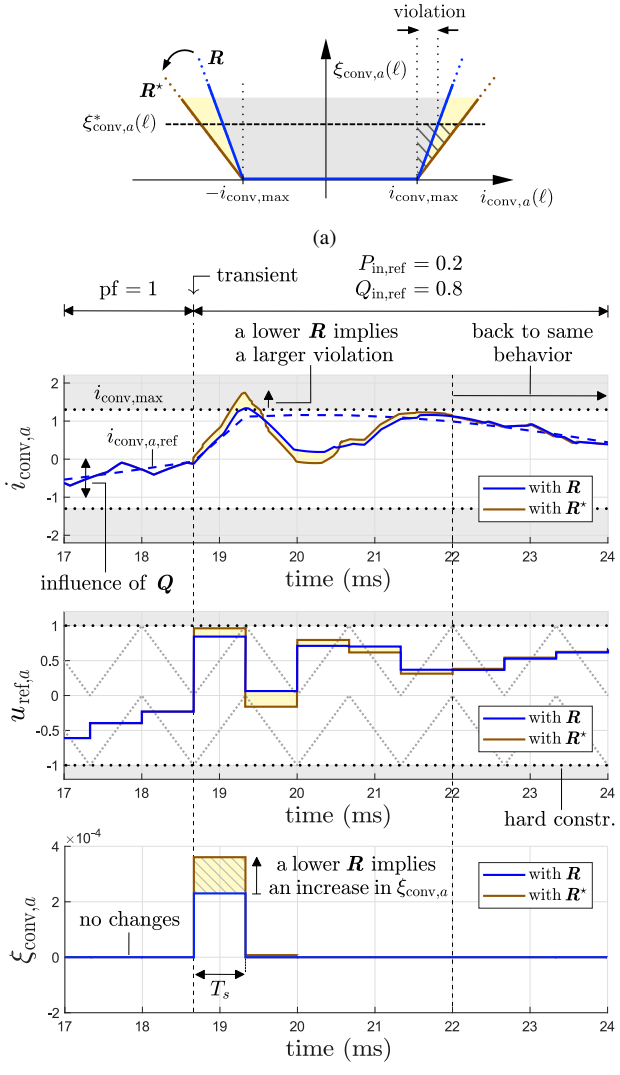

Fig. 10. Impact of tuning of the $\boldsymbol{R}$ weighting matrix on the (a) soft constraints, and (b) dynamic behavior of the proposed indirect MPC algorithm. The same transient scenario as in Fig. 7 is considered, with $\boldsymbol{R} = \mathrm{diag}(10^5, 10^5, 1)$ and $\boldsymbol{R}^\star = \mathrm{diag}(10^2, 10^2, 1)$. For visualization purposes, only one variable is considered, i.e., $i_{\mathrm{conv},a}$, and the corresponding slack variable $\xi_{\mathrm{conv},a}$.

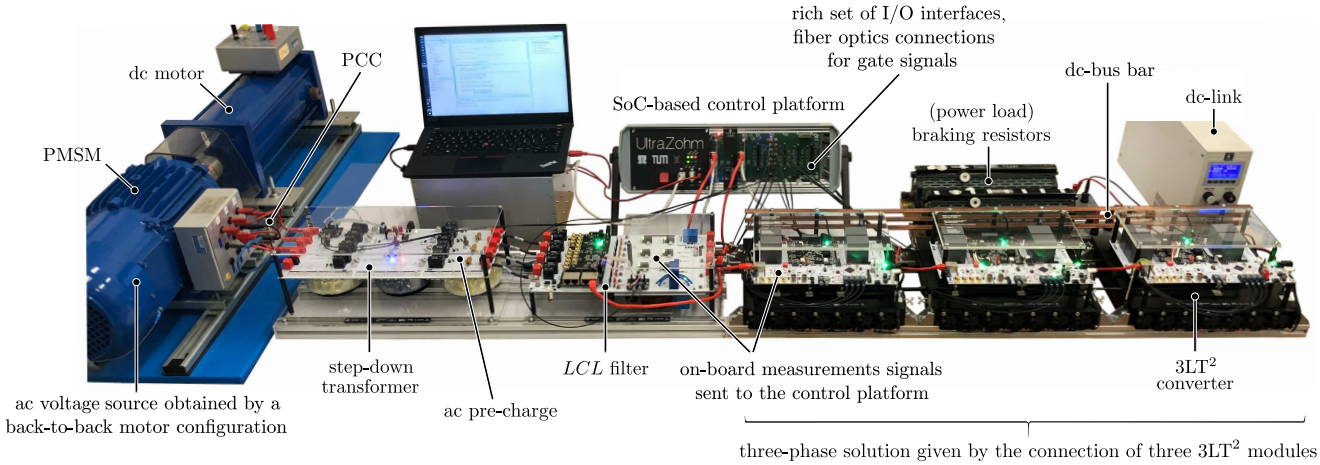

Fig. 11. Self-developed scaled-down experimental setup.

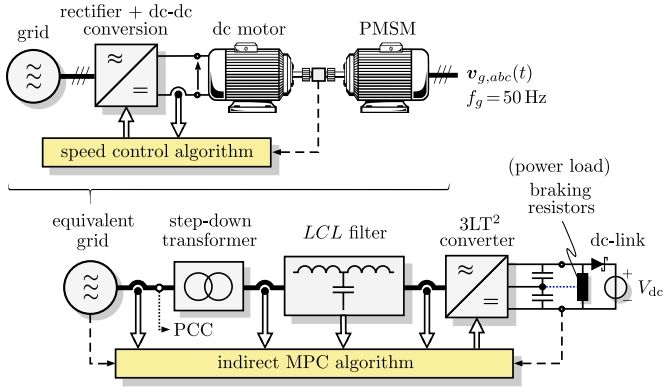

Fig. 12. Visualization of the scaled-down system. The realization of the individual units ("grid", transformer, filter, power converter) and their interconnection are depicted.

TABLE III
LV SYSTEM RATED VALUES AND PARAMETERS

rated voltage V_R	24 V	"grid" inductance L_g	1 mH
rated current I_R	4 A	"grid" resistance R_g	10 mΩ
apparent power S_{sc}	3 kVA	leakage inductance L_t	36 μH
apparent power S_R	$S_{\text{sc}}/k_{\text{sc}}$	leakage resistance R_t	120 mΩ
transformer ratio k	8:1	filter inductance L_{fg}	2 mH
"grid" frequency f_g	50 Hz	filter resistance R_{fg}	25 mΩ
dc-link voltage V_{dc}	40 V	filter inductance L_{fc}	2.2 mH
dc capacitor C_{dc}	1 mF	filter resistancea R_{fc}	25 mΩ
dc resistance R_{dc}	5.33 Ω	filter capacitance C	200 μF
filter resonance f_{res}	308.5 Hz	filter resistance R_c	2 mΩ

a different tuning of $\boldsymbol{R}$ is tested in this section, i.e., $\boldsymbol{R}^\star = \text{diag}(10^2, 10^2, 1)$. In doing so, the dynamic behavior of the indirect MPC scheme is examined during the same transient scenario as in Fig. 7. The results are reported in Fig. 10. As can be seen in the bottom figure of Fig. 10, due to the smaller penalties imposed by $\boldsymbol{R}^\star$ on the slack variables, the MPC algorithm does not try as hard to minimize them. As a result, the controller can make more aggressive decisions that lead to violation of the soft constraints, see the middle and top figures of Fig. 10, respectively. Thus, it can be concluded that a heavy penalization of the slack variables is to be preferred since it can ensure safe operation of the system during transients, while not affecting its steady-state performance.

VII. Experimental Results

In this section, experimental results are provided to validate the effectiveness of the proposed indirect MPC strategy with a real setup. To do so, a scaled-down LV prototype is used, as described in the following.

A. Experimental Setup

To achieve a robust ac voltage that is free of harmonics, the grid voltage source is emulated through a 210 V ac line-to-line (rms), 3 kVA back-to-back system, which consists of a permanent magnet synchronous motor (PMSM) coupled with a dc motor (i.e., the prime mover). The latter is controlled such that a stable three-phase voltage at 50 Hz—acting as the "grid" voltage—appears at the PMSM terminals. Moreover, to be consistent with the simulation studies in Sections V and VI and the assumption of a strong grid, the LV system is designed such that $k_{\text{XR}} \geq 8$ and $k_{\text{sc}} \geq 20$ hold. Finally, to emulate a PLL behavior, an incremental rotary encoder (1024 pulses per cycle) is mounted on the PMSM shaft to measure ω_g.

With regards to the interface between the grid and the power converter, a 300 VA step-down transformer with turn ratio 8:1 is placed between the PMSM (i.e., the "grid") and the power electronic system to provide galvanic isolation. In addition, according to the LCL filter design guidelines described in [3], the inductors L_{fg}, L_{fc}, and capacitor C are designed such that their p.u. values closely match those of the MV setup, thus resulting in a resonance frequency $f_{\text{res}} \approx 308.5$ Hz. In doing so, direct and meaningful comparisons with the simulation results are possible.

As for the power converter, this is a self-developed, three-level T-type (3LT^2) converter.[12] It is important to point out that in terms of switching behavior, the 3LT^2 converter is equivalent to the 3L-NPC one [38], thus the system modeling and controller design presented in Sections III and IV, respectively, hold. Each converter phase leg comprises a Vincotech IGBT 3LT^2 power module (10-FY12NMA160SH01-M820F18) and an isolated gate driver (gate-drive-transformer+ACPL-332J). The converter is supplied by a stiff dc link consisting of two

[12]This design choice was motivated by the fact that, in the LV range, the 3LT^2 converter results in lower power losses compared to a standard 3L-NPC converter [38].

voltage power supplies connected in series that provide $V_{\rm dc}/2$ each. Two (equal) braking resistors are placed in parallel to the output capacitor banks to allow for the required power transfer. The complete LV setup is shown in Fig. 11, while the system rated values and parameters are summarized in Table III. Moreover, Fig. 12 shows a graphical representation of the setup.

The control algorithm is implemented on a customized control platform based on a Xilinx multiple processor system-on-chip field-programmable gate array (MPSoC FPGA) [39]. The hardware, i.e., Zynq UltraScale+ MPSoC ZU9EG, contains both an ARM-based processing system (PS) in the form of two ARM processors (A53 and R5), and the programmable logic (PL) in the form of FPGA fabric (more than 2500 DSP slices). The PS is programmed using C while the PL was configured using VHDL.

Finally, regarding the measurements, current (e.g., LEM HLSR 20-P) and voltage on-board sensors are used to measure the system state and dc-link voltage. These measurements are sampled and directly fed into the MPSoC-based control platform. As for the gating signals resulting from the 3L CB-PWM stage, they are sent to the 3LT^2 converter via fiber optic cables (HFBR-1521Z and 2521Z links).

B. Embedded Implementation and Execution

As explained in the sequel of this section, the MPC algorithm is running on the ARM R5 (500 MHz clock) of the PS, while the ARM A53 (1.2 GHz clock) attends "housekeeping" tasks, such as the initialization of the FPGA, data logging and external communication, i.e., tasks that are not directly relevant to the controller. The 3L CB-PWM stage, interlock-time generation, and analog-to-digital converter (ADC) input processing are handled by the PL. Both the ADCs and modulator are implemented as intellectual property (IP) cores with a 100 MHz clock, exploiting the parallelization abilities of the FPGA.

The distributed measurements—i.e., the state $\boldsymbol{x}(k)$—are read through ADC modules (MAX11331) with 12 bit resolution, sent to the PL (via single-ended SPI) at the high sample rate of 125 ksps, and transferred from the PL to the PS via the dedicated advanced extensible interface (AXI). The latter is also used by the modulator to communicate with the PS, e.g., to get the modulating signal. At each sampling interval T_s, the ADCs are triggered with a start-of-conversion (SOC) which is synchronized with the (upper and lower) peaks of the triangular carrier. The end-of-conversion (EOC) of the ADCs triggers the execution of the indirect MPC algorithm, consisting of a preprocessing stage and the solution of the QP (31), in the PS.

Since the aim is to have the same switching frequency as in Section V, it means that the chosen sampling interval is $T_s = T_c/2 = 666.67\,\mu$s. Hence, the MPC algorithm needs to be executed in real time in less than the aforementioned T_s. Given the relatively small size of the QP (31), there is ample time to solve it (i.e., to find the optimal modulating signal) without sacrificing optimality. This also enables the implementation of the QP on the ARM processor (in the R5), which greatly simplifies the implementation procedure since the algorithm can be programmed in C and the operations performed in floating-point arithmetic. These aspects, combined with the inherent interrupt-service routine (ISR), make easier the control algorithms synthesis, thus, reducing the development/validation effort.

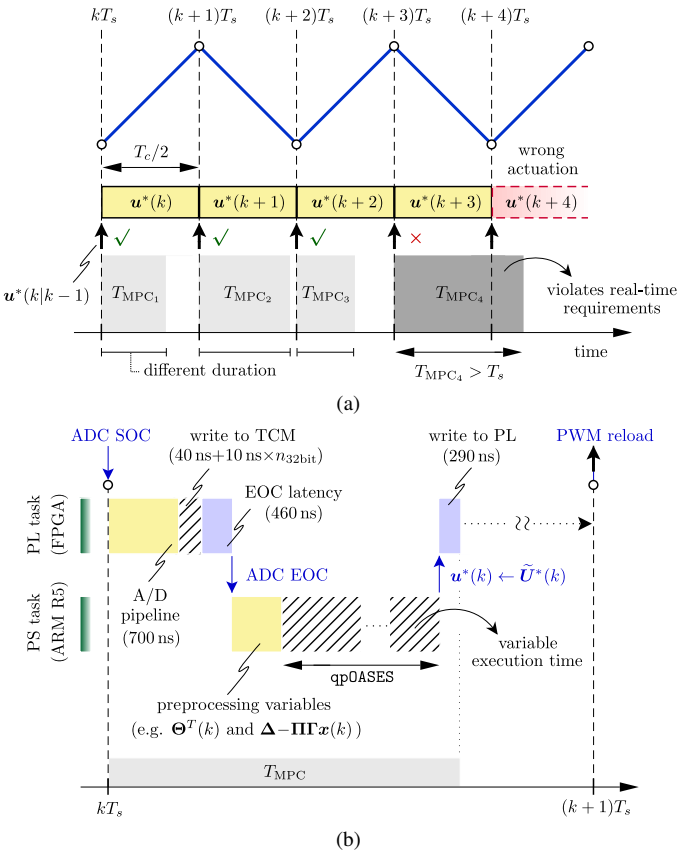

Fig. 13. Description of the algorithm execution/scheduling by highlighting the event sequence within T_s. (a) A longer $T_{\rm QP}$ implies a larger number of iterations of the QP solver; the longest one defines the worst-case execution time. (b) All computations must be executed within T_s i.e., $T_{\rm MPC} < T_s$, to achieve real-time certification.

Given the above, an off-the-self solver can be employed to solve the QP underlying indirect MPC in a computationally efficient manner [14, Section IV]. A solver that has been gaining popularity in the power electronics community is `qpOASES` [29], which is based on an online parametric AS algorithm and is available as open-source software. Its features, e.g., the fact that its source code is written in C/C++ with dense linear algebra and provided as a self-contained software package as well as that it can be directly linked to plain C code, make `qpOASES` suitable for the R5 implementation in the given MPSoC.

Since the aforementioned tasks have to be performed in real time, Fig. 13 depicts a simplified scheduling of the subsequent calls of the indirect MPC algorithm running in the chosen embedded calculation platform. The event sequence, executed within T_s, is synchronized with the PL interrupt triggers and is scheduled as follows.

- At the beginning of T_s, the ADCs are triggered with a SOC interrupt by the triangular carrier. The SPI clock

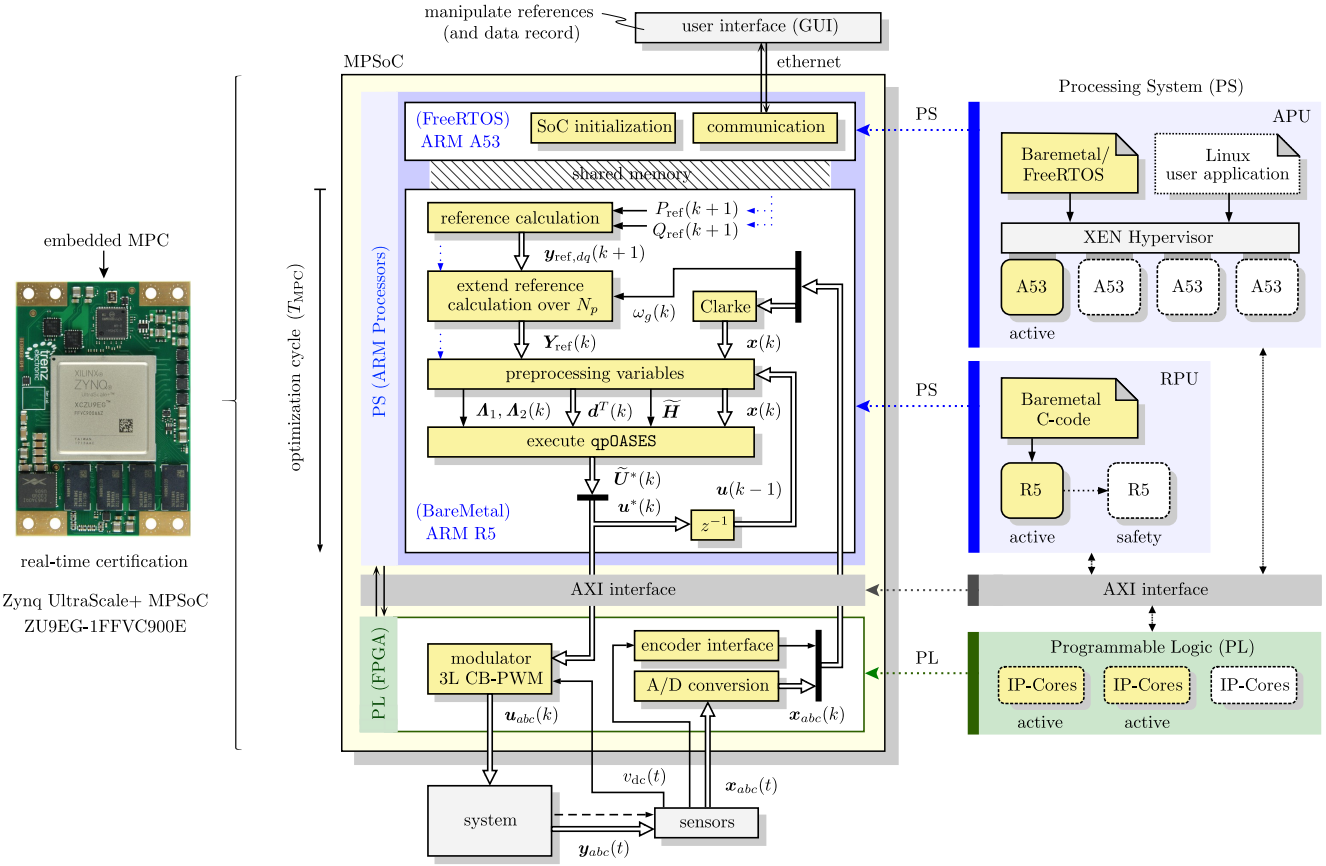

Fig. 14. FPGA-based MPSoC structure for the implementation of the proposed indirect MPC algorithm. The blue dotted lines denote variables loaded from the shared memory (e.g., off-line parameters/matrices). The related software stack utilization is reported on the right-hand side, where the application processing unit (APU) and real-time processing unit (RPU) are shown.

runs at 20 MHz and the PL takes 700 ns from the rising edge of the trigger until the data are sampled and converted to their real value in fixed point. The sampling is done in parallel, which implies that this latency is independent of the number of ADCs. Once the data are sampled, they are sent to the tightly coupled memory (TCM) via AXI interface; the write transaction has 40 ns of overhead and takes 10 ns for each 32-bit value.

- When the write transaction is completed, an EOC interrupt from the PL to PS triggers the control routine executed on the R5. The EOC has a latency of 460 ns. The total overhead to sample, convert, and send the measurements to the PS as well as trigger the control interrupt routine is $\approx 2\,\mu$s. The timing required for this point and the previous one is stated as $T_{\text{PL}\to\text{PS}}$.
- Before solving (31), a preprocessing stage is required to formulate it. Since matrices $\widetilde{\boldsymbol{H}}$, $\boldsymbol{\Omega}$, $\boldsymbol{0}_{6N_p\times 3N_p}$, $\boldsymbol{\Pi}$, $\boldsymbol{\Upsilon}$, $\boldsymbol{Z}$, $\boldsymbol{1}_{6N_p}$, $\boldsymbol{\Delta}$, and $\boldsymbol{\Gamma}$ are time-invariant, they can be computed offline for a given horizon N_p and given as an input to the PS. The calculation of the reference vector over the horizon of N_p time steps $\boldsymbol{Y}_{\text{ref}}(k)$ as well as that of $\boldsymbol{\Theta}^T(k)$—necessary for the computation of $\boldsymbol{d}^T(k)$—are done online in the PS. The same applies to the update of constraint $\boldsymbol{\Delta}-\boldsymbol{\Pi}\boldsymbol{\Gamma}\boldsymbol{x}(k)$. The preprocessing timing is stated as T_{pre}.
- Once (31) is formulated, qpOASES is called. The number of AS iterations required to find the solution depends not only on the size of the problem, but also on the operating point (i.e., initial conditions/guess). Thus, the solver execution time T_{QP}, which defines the time required by the solver to conclude to the optimal solution $\widetilde{\boldsymbol{U}}^*(k)$, may differ from cycle to cycle. However, T_{QP} is expected to be sufficiently smaller than T_s to avoid feasibility issues. A timing analysis of the *worst-case* scenario, which is the most relevant case from implementation point of view, is provided in Section VII-D.
- In a last step, the optimal modulating signal $\boldsymbol{u}^*(k)$ is extracted from $\widetilde{\boldsymbol{U}}^*(k)$. This is both stored to be used in the next iteration of the controller (as $\boldsymbol{u}^*(k-1)$) and sent from the PS to PL via AXI interface. The writing transaction from PS to the 32-bit FPGA registers takes 290 ns on average. These data are stored in the PL. Note that even if $\boldsymbol{u}^*(k)$ may be available before the end of T_s, the 3L CB-PWM modulator inputs are loaded only at the discrete time steps $k+1$, $k+2$, ... Finally, the resulting gating signals are computed according to the modulator IP clock (i.e., 100 MHz).

The execution steps of the proposed indirect MPC algorithm are summarized in the flowchart presented in Fig. 14. Therein, the matrices $\boldsymbol{\Lambda}_1$ and $\boldsymbol{\Lambda}_2(k)$ are introduced to simplify the notation. These matrices are defined in the appendix. Finally, the overall embedded MPC execution time is stated as T_{MPC}.

C. Performance Assessment

For direct comparison with the simulation results presented in Section V, the same steady-state operating point is used, namely, $P_{\mathrm{in,ref}} = 1\,\mathrm{p.u.}$ and $Q_{\mathrm{in,ref}} = 0\,\mathrm{p.u.}$ (i.e., $\mathrm{pf} = 1$). Likewise, the dynamic performance is tested under the same transient scenario, i.e., $P_{\mathrm{in,ref}}$ is changed from 1 to $0.2\,\mathrm{p.u.}$ and back to $1\,\mathrm{p.u.}$ while $Q_{\mathrm{in,ref}}$ is changed from 0 to $0.8\,\mathrm{p.u.}$ and back to $0\,\mathrm{p.u.}$ at the same time instants. Moreover, the carrier frequency is—as in Section V—equal to $750\,\mathrm{Hz}$. As for the controller, a four-step horizon is used ($N_p = 4$). The entries of $\boldsymbol{Q}$, $\boldsymbol{R}$, and λ_u are the same as those in Section V. Finally, the soft constraints on all output variables are set equal to $1.25\,\mathrm{p.u.}$

The steady-state and transient performance of the embedded indirect MPC with the LV prototype presented in Section VII-A is shown in Fig. 15. More specifically, Fig. 15(a) shows the closed-loop behavior of indirect MPC without soft constraints, whereas Fig. 15(b) depicts the system response when the aforementioned constraints are included in the control problem. As is the case with grid-tied converters, the dc link needs to be appropriately pre-charged before normal operation can be initiated. To this end, a pre-charge circuit (i.e., soft starter) is introduced between the step-down transformer and the LCL filter to limit the dc-link charging current, see Fig. 11. In this interval the system is operated as passive rectifier and the MPC algorithm is inactive, see the light yellow-shaded areas in Fig. 15 for $t < 150\,\mathrm{ms}$. At time instant $t = 150\,\mathrm{ms}$, the pre-charge circuit is bypassed and the indirect MPC is activated. The initial operating point corresponds to $\mathrm{pf} = 1$, and the system operates under this condition until $t = 173\,\mathrm{ms}$. At that instant, $P_{\mathrm{in,ref}}$ is changed from 1 to $0.2\,\mathrm{p.u.}$ and $Q_{\mathrm{in,ref}}$ is changed from 0 to $0.8\,\mathrm{p.u.}$ Finally, the operating point is changed back to $\mathrm{pf} = 1$ at $t = 180\,\mathrm{ms}$.

As can be seen, regardless of the operating point and the MPC method used (i.e., without or with soft constraints), all output variables $\boldsymbol{y}_{abc}$ accurately track their reference values $\boldsymbol{y}_{\mathrm{ref},abc}$. This occurs despite operation at the low switching frequency of $f_{\mathrm{sw}} = 400\,\mathrm{Hz}$, which is very close to the resonance frequency $f_{\mathrm{res}} = 308.5\,\mathrm{Hz}$. Therefore, it can be claimed that the full-state information of MPC, combined with the adopted long horizon of four time steps, equips the control algorithm with an active damping capability. The steady-state superior performance of the proposed controller is also highlighted in Fig. 16, where the grid current and PCC voltage harmonic spectra are depicted. It can be observed that the TDD of both variables is low and well within the limits imposed by the relevant grid standards. In addition, as also indicated by the simulation results in Fig. 8, MPC can produce lower harmonics than the conventional SVM method.

Although the steady-state behavior of both constrained and unconstrained MPC is—as expected—the same, since no constraints are active, the dynamic behavior of the two methods is significantly different. Specifically, as can be seen in Fig. 15(a), the variables $\boldsymbol{i}_{\mathrm{conv}}$ and $\boldsymbol{v}_c$ exhibit significant overshoots during transients, violating the associated trip levels. For instance, the transition from pre-charge to steady-state operation is particularly stressful for the filter capacitors which are affected by the instantaneous large load demand. The manifested peak values of $v_{c,c} \approx 2\,\mathrm{p.u.}$ and $v_{c,a} \approx -2\,\mathrm{p.u.}$ are 79% above/below $\pm v_{c,\max} = \pm 1.25\,\mathrm{p.u.}$, respectively, with an overload interval of $\approx 2.8\,\mathrm{ms}$. Likewise, stressful peaks are experienced during the other transient scenarios examined, and in line with the presented simulations, e.g., $i_{\mathrm{conv},a} \approx 1.8\,\mathrm{p.u.}$, $i_{\mathrm{conv},c} \approx -1.6\,\mathrm{p.u.}$, and $v_{c,c} \approx -1.88\,\mathrm{p.u.}$

On the other hand, when MPC is implemented with soft constraints, all controlled variables remain mostly within their bounds, with only minute violations occurring due to the very low switching frequency, and thus less frequent control actions. Notwithstanding the foregoing, both overcurrents and overvoltages are prevented thanks to the proposed MPC problem formulation. As a result, the hardware of the system is protected from potential damage and a potential system interruption due to converter trips is prevented.

D. Timing Analysis and Worst-Case Computational Cost

Considering the relevance of "real-time certification" for MPC algorithms, a worst-case computational cost analysis is required to gain insight into the computational requirements and feasibility of the proposed indirect MPC strategy. To this end, the *worst-case execution time* T_{wrt} needs to be examined. Indeed, $T_{\mathrm{wrt}} < T_s$ holds if the coded firmware runs reliably within each cycle.

As defined in Section VII-B, the embedded MPC execution time T_{MPC} is defined as

$$T_{\mathrm{MPC}} = T_{\mathrm{QP}} + T_{\mathrm{ovr}}\,, \tag{32}$$

where $T_{\mathrm{ovr}} \approx T_{\mathrm{PL}\to\mathrm{PS}} + T_{\mathrm{pre}} + T_{\mathrm{PS}\to\mathrm{PL}}$, with $T_{\mathrm{PL}\to\mathrm{PS}}$ and $T_{\mathrm{PS}\to\mathrm{PL}}$ being constant. Given the prediction horizon steps N_p, both $\boldsymbol{Y}_{\mathrm{ref}}(k)$ and $\boldsymbol{\Theta}^T(k)$ are size-invariant, thus, the time T_{pre} required for scaling and matrix factorization is almost constant. As for T_{QP}, this depends on the number of iterations n_{iter} of the QP solver. This number, in turn, depends on the number of activated constraints n_{costr} (either hard or soft) at each execution of `qpOASES`, i.e. if $n_{\mathrm{costr}} \geq 1$ then $n_{\mathrm{iter}} \geq 1$. Hence, given the above and (32), it is evident that the maximum execution time T_{wrt} corresponds to the case where the maximum number of iterations is required.

Given the MPSoC real-time implementation and the recorded data provided in Fig. 15, the associated real-time computational effort in terms of n_{costr}, n_{iter}, and T_{QP} is shown in Fig. 17. As can be seen, the transitions from the pre-charge state to $\mathrm{pf} = 1$ and from $P_{\mathrm{in,ref}} = 0.2\,\mathrm{p.u.}$ and $Q_{\mathrm{in,ref}} = 0.8\,\mathrm{p.u.}$ back to $\mathrm{pf} = 1$ are the most computationally demanding cases. At $t = 150\,\mathrm{ms}$, the embedded MPC algorithm requires about $T_{\mathrm{MPC}} \approx 400\,\mu\mathrm{s}$, with $n_{\mathrm{costr}} = 6$ and $n_{\mathrm{iter}} = 10$, to calculate the solution $\widetilde{\boldsymbol{U}}^*(k)$ and then apply the optimal three-phase switch positions $\boldsymbol{u}^*_{abc}(k)$ to the converter. Given that $T_s = 666.67\,\mu\mathrm{s}$, it can be deduced that the total execution time is within the available run-time as it is about 60% of T_s. Nevertheless, the most computationally demanding scenario is when the desired power factor becomes again equal to one at $t = 181\,\mathrm{ms}$. As can be seen in Fig. 15, several (both state and input) constraints are activated during this transients. Specifically, $n_{\mathrm{costr}} = 7$ constraints are activated,

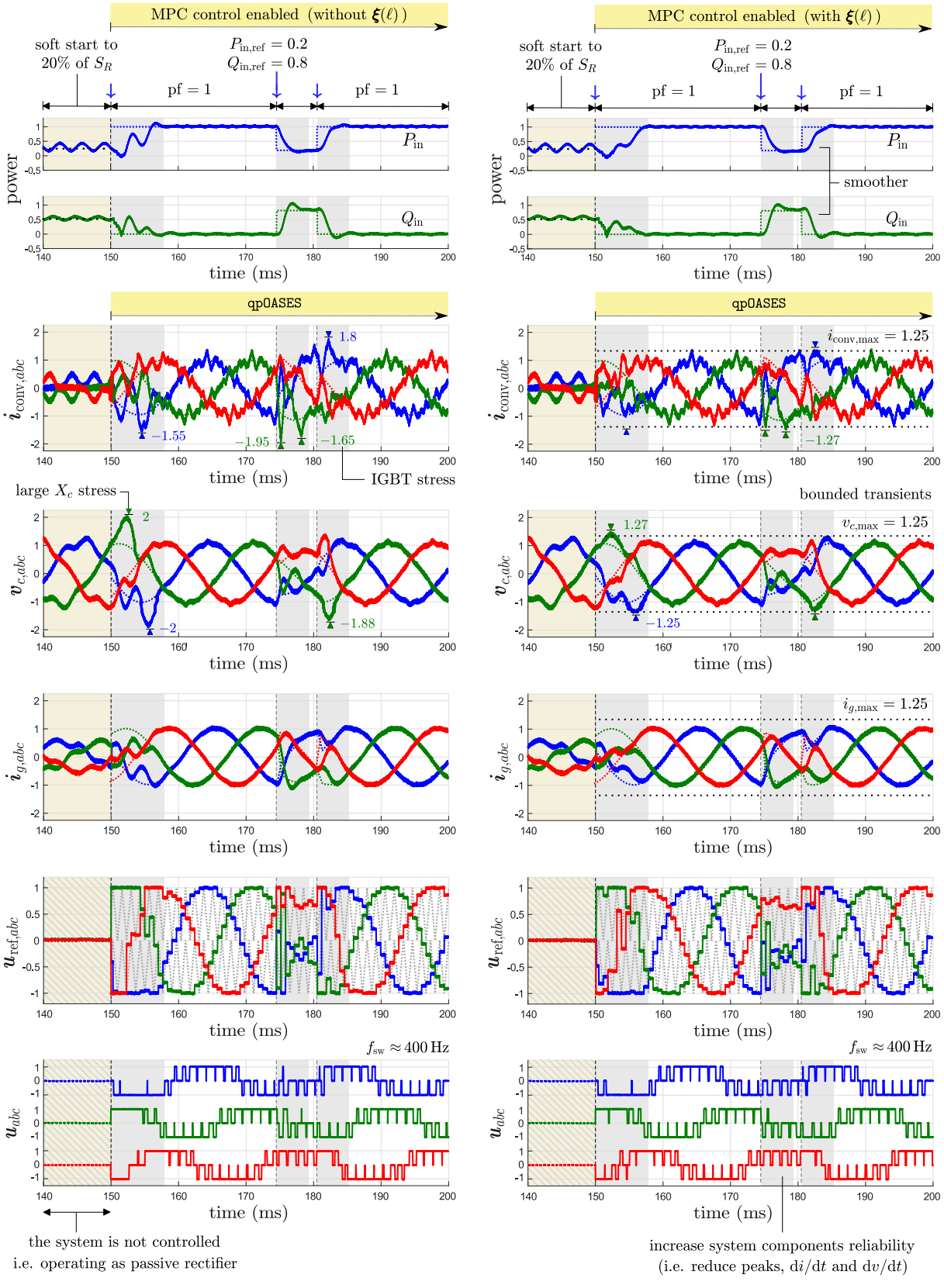

Fig. 15. Experimental waveforms produced by indirect MPC with $N_p = 4$, when the soft constraints are (a) not included, and (b) included.

resulting in $n_{\text{iter}} = 13$ iterations, and thus a total execution time about 67.5% of T_s since $T_{\text{MPC}} = T_{\text{wrt}} \approx 450\,\mu$s. As for the transient at $t = 174$ ms, this is less stressful because only one constraint is activated, namely the one that relates to $i_{\text{conv},c}$, see Fig. 15(a). On the other hand, when no constraints are active ($n_{\text{costr}} = 0$), the unconstrained solution of (31) is feasible implying that no iterations are required. This greatly reduces the computational effort at steady-state operation. As a

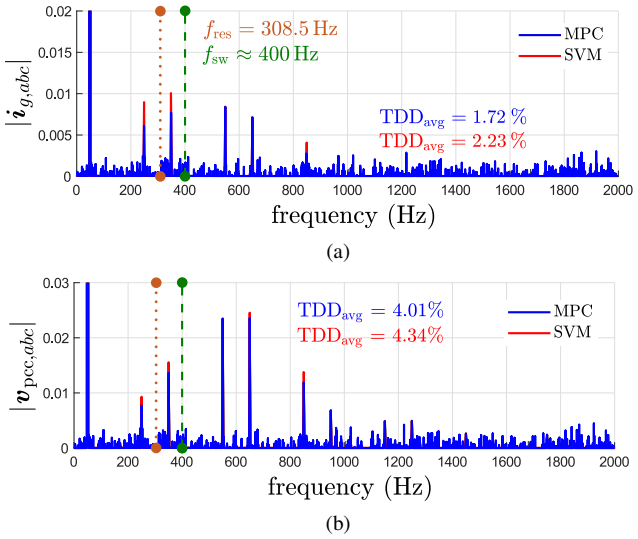

Fig. 16. Experimental results: Harmonic spectra of the (a) grid current, and (b) PCC voltage. The limits imposed by the IEEE 519 and IEC 61000-2-4 standards, respectively, are met.

result, the *average execution time* T_{avg} of the embedded MPC algorithm is as low as $T_{\mathrm{avg}} \approx 150\,\mu$s, i.e., only 22.5% of T_s.

Based on the mentioned required execution times, it can be concluded that the discussed MPSoC implementation meets the needs of the proposed MPC algorithm and guarantees that the solution to the problem (31) is always found. As a result, the best possible performance of the power electronic system is ensured, as indicated by the experimental results, see Section VII-C.

VIII. Conclusions

This paper presented a long-horizon MPC algorithm with a modulator for a 3L-NPC converter connected to the grid via an intermediate LCL filter. By appropriately formulating the optimization problem underlying indirect MPC as a multi-criterion QP, the grid and converter currents as well as the filter capacitor voltage can be simultaneously and successfully controlled, while the relevant grid standards, e.g., the IEEE 519 and IEC 6000-2-4 standards, can be met. The above can be achieved while respecting the trip/protection levels of the system, thus enhancing the converter reliability. To realize the latter, soft constraints are included into the optimization problem, the violation of which is minimized. To this end, MPC computes the optimal three-phase modulating signal—subsequently fed into a CB-PWM stage—that satisfies all the aforementioned objectives and ensures smooth operation of the system. Finally, a relatively long prediction horizon is employed to improve the closed-loop system performance and avoid potential stability issues. As a result, the converter can be operated at a switching frequency of a few hundred Hz, very close to the resonance frequency, without requiring an additional active damping loop. In doing so, the power losses can be kept low, while the controller structure is greatly simplified.

To demonstrate the effectiveness of the proposed strategy, simulations based on an MV power electronic system as well as experiments with an LV prototype were performed both

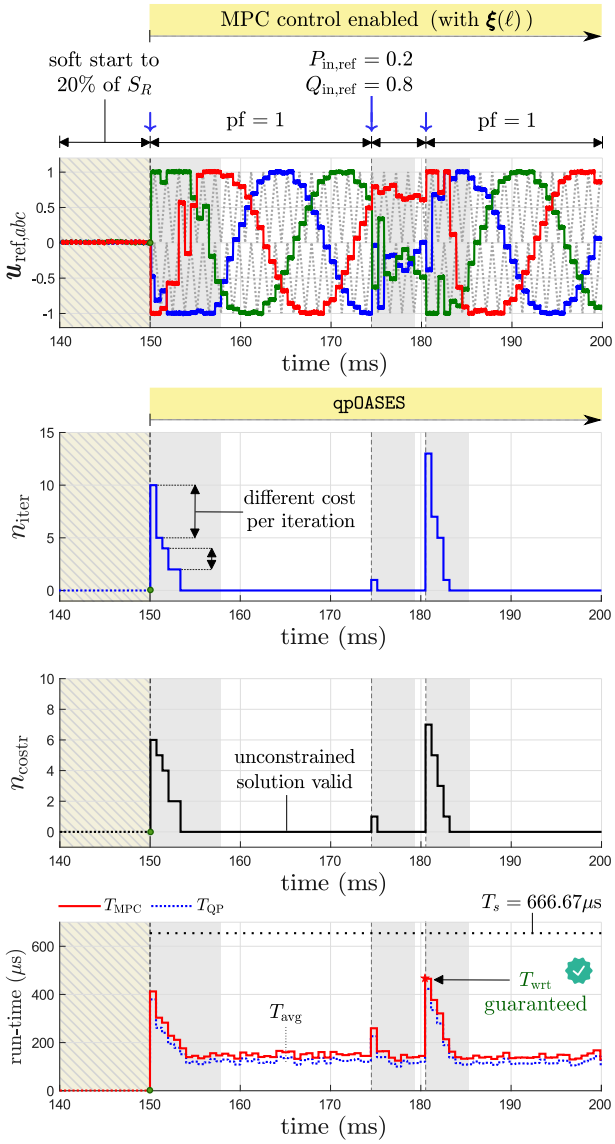

Fig. 17. Analysis of the real-time computational effort of the proposed indirect MPC algorithm in terms of n_{costr}, n_{iter}, and T_{MPC}.

at steady-state and transient operating conditions. As shown, the proposed MPC scheme outperforms conventional control and modulation methods (e.g., SVM) at steady state, where a low grid current TDD is achieved, while operation within the safe operating area is ensured during power transients. These features, make the developed MPC framework suitable for high-power applications.

Appendix

The matrices $\boldsymbol{\Upsilon}$, $\boldsymbol{E}$, $\boldsymbol{\Gamma}$, and $\boldsymbol{S}$ in (25) are

$$\boldsymbol{\Upsilon} = \begin{bmatrix} \boldsymbol{CB} & \boldsymbol{0}_{6\times3} & \cdots & \boldsymbol{0}_{6\times3} \\ \boldsymbol{CAB} & \boldsymbol{CB} & \cdots & \boldsymbol{0}_{6\times3} \\ \vdots & \vdots & \cdots & \vdots \\ \boldsymbol{CA}^{N_p-1}\boldsymbol{B} & \boldsymbol{CA}^{N_p-2}\boldsymbol{B} & \cdots & \boldsymbol{CB} \end{bmatrix}, \boldsymbol{E} = \begin{bmatrix} \boldsymbol{I}_3 \\ \boldsymbol{0}_{3\times3} \\ \boldsymbol{0}_{3\times3} \\ \vdots \\ \boldsymbol{0}_{3\times3} \end{bmatrix},$$

$$\boldsymbol{\Gamma} = \begin{bmatrix} \boldsymbol{CA} \\ \boldsymbol{CA}^2 \\ \vdots \\ \boldsymbol{CA}^{N_p} \end{bmatrix}, \; \boldsymbol{S} = \begin{bmatrix} \boldsymbol{I}_3 & \boldsymbol{0}_{3\times 3} & \cdots & \boldsymbol{0}_{3\times 3} \\ -\boldsymbol{I}_3 & \boldsymbol{I}_3 & \cdots & \boldsymbol{0}_{3\times 3} \\ \boldsymbol{0}_{3\times 3} & -\boldsymbol{I}_3 & \cdots & \boldsymbol{0}_{3\times 3} \\ \vdots & \vdots & \cdots & \vdots \\ \boldsymbol{0}_{3\times 3} & \boldsymbol{0}_{3\times 3} & \cdots & \boldsymbol{I}_3 \end{bmatrix}.$$

which are of dimensions $6N_p \times 3N_p$, $3N_p \times 3$, $6N_p \times 8$, and $3N_p \times 3N_p$, respectively. Moreover, matrices $\boldsymbol{\Lambda}_1$ and $\boldsymbol{\Lambda}_2(k)$ in Fig. 14 are defined as

$$\boldsymbol{\Lambda}_1 = \begin{bmatrix} \boldsymbol{\Omega} & \boldsymbol{0}_{6N_p \times 3N_p} \\ \boldsymbol{\Pi\Upsilon} & \boldsymbol{Z} \end{bmatrix}, \quad \boldsymbol{\Lambda}_2(k) = \begin{bmatrix} \boldsymbol{1}_{6N_p} \\ \boldsymbol{\Delta} - \boldsymbol{\Pi\Gamma} \boldsymbol{x}(k) \end{bmatrix}.$$

ACKNOWLEDGMENTS

The authors would like to thank E. Liegmann of Technical University of Munich, Germany, for the help on real-time implementation, and the companies ePEBB^s Srl, Italy, and Zohm Control GmbH, Germany, for their support with the development and testing of the experimental setup.

REFERENCES

[1] IEEE Std 519-2014 (Revision of IEEE Std 519-1992), "IEEE recommended practices and requirements for harmonic control in electrical power systems," pp. 1–29, Jun. 2014.

[2] IEC 61000-2-4, "Electromagnetic compatibility (EMC)—part 2-4: Environment—compatibility levels in industrial plants for low-frequency conducted disturbances," Sep. 2002.

[3] M. Liserre, F. Blaabjerg, and S. Hansen, "Design and control of an LCL-filter-based three-phase active rectifier," *IEEE Trans. Ind. Appl.*, vol. 41, no. 5, pp. 1281–1291, Sep./Oct. 2005.

[4] P. C. Loh and D. Holmes, "Analysis of multiloop control strategies for LC/CL/LCL-filtered voltage-source and current-source inverters," *IEEE Trans. Ind. Appl.*, vol. 41, no. 2, pp. 644–654, Mar./Apr. 2005.

[5] M. P. Kazmierkowski, R. Krishnan, and F. Blaabjerg, *Control in power electronics: Selected problems*. New York, NY, USA: Academic Press, 2002.

[6] M. Malinowski, M. P. Kazmierkowski, S. Hansen, F. Blaabjerg, and G. D. Marques, "Virtual-flux-based direct power control of three-phase pwm rectifiers," *IEEE Trans. Ind. Appl.*, vol. 37, no. 4, pp. 1019–1027, Jul./Aug. 2001.

[7] S. Rivera, S. Kouro, B. Wu, S. Alepuz, M. Malinowski, P. Cortes, and J. Rodriguez, "Multilevel direct power control—A generalized approach for grid-tied multilevel converter applications," *IEEE Trans. Power Electron.*, vol. 29, no. 10, pp. 5592–5604, Oct. 2014.

[8] S. Yan, Y. Yang, S. Y. Hui, and F. Blaabjerg, "A review on direct power control of pulsewidth modulation converters," *IEEE Trans. Power Electron.*, vol. 36, no. 10, pp. 11 984–12 007, Oct. 2021.

[9] J. Dannehl, M. Liserre, and F. W. Fuchs, "Filter-based active damping of voltage source converters with LCL filter," *IEEE Trans. Ind. Electron.*, vol. 58, no. 8, pp. 3623–3633, Aug. 2011.

[10] J. Dannehl, F. W. Fuchs, S. Hansen, and P. B. Thøgersen, "Investigation of active damping approaches for PI-based current control of grid-connected pulse width modulation converters with LCL filters," *IEEE Trans. Ind. Appl.*, vol. 46, no. 4, pp. 1509–1517, Jul./Aug. 2010.

[11] P. Cortés, M. P. Kazmierkowski, R. M. Kennel, D. E. Quevedo, and J. Rodriguez, "Predictive control in power electronics and drives," *IEEE Trans. Ind. Electron.*, vol. 55, no. 12, pp. 4312–4324, Dec. 2008.

[12] J. Rodriguez, M. P. Kazmierkowski, J. R. Espinoza, P. Zanchetta, H. Abu-Rub, H. A. Young, and C. A. Rojas, "State of the art of finite control set model predictive control in power electronics," *IEEE Trans. Ind. Informat.*, vol. 9, no. 2, pp. 1003–1016, May 2013.

[13] T. Geyer, *Model predictive control of high power converters and industrial drives*. Hoboken, NJ, USA: Wiley, 2016.

[14] P. Karamanakos, E. Liegmann, T. Geyer, and R. Kennel, "Model predictive control of power electronic systems: Methods, results, and challenges," *IEEE Open J. Ind. Appl.*, vol. 1, pp. 95–114, 2020.

[15] P. Karamanakos and T. Geyer, "Guidelines for the design of finite control set model predictive controllers," *IEEE Trans. Power Electron.*, vol. 35, no. 7, pp. 7434–7450, Jul. 2020.

[16] D. Pérez-Estévez and J. Doval-Gandoy, "A finite-control-set linear current controller with fast transient response and low switching frequency for grid-tied inverters," *IEEE Trans. Ind. Appl.*, vol. 56, no. 6, pp. 6546–6564, Nov./Dec. 2020.

[17] D. G. Holmes and T. A. Lipo, *Pulse width modulation for power converters: Principles and practice*. Piscataway, NJ, USA: IEEE Press, 2003.

[18] S. Mariéthoz and M. Morari, "Explicit model-predictive control of a PWM inverter with an LCL filter," *IEEE Trans. Ind. Electron.*, vol. 56, no. 2, pp. 389–399, Feb. 2009.

[19] S. Vazquez, C. Montero, C. Bordons, and L. G. Franquelo, "Model predictive control of a VSI with long prediction horizon," in *Proc. IEEE Int. Symp. Ind. Electron.*, Gdansk, Poland, Jun. 2011, pp. 1805–1810.

[20] C. M. Hackl, "MPC with analytical solution and integral error feedback for LTI MIMO systems and its application to current control of grid-connected power converters with LCL-filter," in *Proc. IEEE Int. Symp. Pred. Control of Elect. Drives and Power Electron.*, Valparaíso, Chile, Oct. 2015, pp. 61–66.

[21] H. T. Nguyen, E.-K. Kim, I.-P. Kim, H. H. Choi, and J.-W. Jung, "Model predictive control with modulated optimal vector for a three-phase inverter with an LC filter," *IEEE Trans. Power Electron.*, vol. 33, no. 3, pp. 2690–2703, Mar. 2018.

[22] A. Sadie, T. Mouton, M. Dorfling, and T. Geyer, "Model predictive control with space-vector modulation for a grid-connected converter with an LCL-filter," in *Proc. Eur. Power Electron. Conf.*, Genova, Italy, Sep. 2019, pp. P.1–P.9.

[23] M. Rossi, P. Karamanakos, and F. Castelli-Dezza, "Indirect model predictive control for a grid-tied three-level neutral point clamped converter with an LCL filter," in *Proc. IEEE Energy Convers. Congr. Expo.*, Detroit, MI, USA, Oct. 2020, pp. 6245–6252.

[24] P. Karamanakos, T. Geyer, N. Oikonomou, F. D. Kieferndorf, and S. Manias, "Direct model predictive control: A review of strategies that achieve long prediction intervals for power electronics," *IEEE Ind. Electron. Mag.*, vol. 8, no. 1, pp. 32–43, Mar. 2014.

[25] T. Geyer, P. Karamanakos, and R. Kennel, "On the benefit of long-horizon direct model predictive control for drives with LC filters," in *Proc. IEEE Energy Convers. Congr. Expo.*, Pittsburgh, PA, USA, Sep. 2014, pp. 3520–3527.

[26] A. A. Rockhill, M. Liserre, R. Teodorescu, and P. Rodriguez, "Grid-filter design for a multimegawatt medium-voltage voltage-source inverter," *IEEE Trans. Ind. Electron.*, vol. 58, no. 4, pp. 1205–1217, Apr. 2011.

[27] B. Hauska, H. J. Ferreau, and M. Diehl, "An auto-generated real-time iteration algorithm for nonlinear MPC in the microsecond range," *Automatica*, vol. 47, no. 10, pp. 2279–2285, Oct. 2011.

[28] H. Peyrl, A. Zanarini, T. Besselmann, J. Liu, and M.-A. Boéchat, "Parallel implementations of the fast gradient method for high-speed MPC," *Control Eng. Pract.*, vol. 33, pp. 22–34, Dec. 2014.

[29] H. J. Ferreau, C. Kirches, A. Potschka, H. G. Bock, and M. Diehl, "qpOASES: A parametric active-set algorithm for quadratic programming," *Math. Program. Comp.*, vol. 6, no. 4, pp. 327–363, Dec. 2014.

[30] S. Yang, A. Bryant, P. Mawby, D. Xiang, L. Ran, and P. Tavner, "An industry-based survey of reliability in power electronic converters," *IEEE Trans. Ind. Appl*, vol. 47, no. 3, pp. 1441–1451, May/Jun. 2011.

[31] D. Zhou, H. Wang, and F. Blaabjerg, "Reactive power impacts on LCL filter capacitor lifetime in grid-connected inverter," *IEEE Open J. Power Electron.*, vol. 1, pp. 139–148, 2020.

[32] D. Q. Mayne, J. B. Rawlings, C. V. Rao, and P. O. M. Scokaert, "Constrained model predictive control: Stability and optimality," *Automatica*, vol. 36, no. 6, pp. 789–814, Jun. 2000.

[33] G. Darivianakis, T. Geyer, and W. van der Merwe, "Model predictive current control of modular multilevel converters," in *Proc. IEEE Energy Convers. Congr. Expo.*, Pittsburgh, PA, USA, Sep. 2014, pp. 5016–5023.

[34] S. Boyd and L. Vandenberghe, *Convex optimization*. Cambridge, UK: Cambridge Univ. Press, 2004.

[35] J. B. Rawlings and D. Q. Mayne, *Model predictive control: Theory and design*. Madison, WI, USA: Nob Hill, 2009.

[36] D. Kouzoupis, A. Zanelli, H. Peyrl, and H. J. Ferreau, "Towards proper assessment of QP algorithms for embedded model predictive control," in *Proc. Eur. Control Conf.*, Linz, Austria, Jul 2015, pp. 2609–2616.

[37] P. Karamanakos, M. Nahalparvari, and T. Geyer, "Fixed switching frequency direct model predictive control with continuous and discontinuous modulation for grid-tied converters with LCL filters," *IEEE Trans. Control Syst. Technol.*, vol. 29, no. 4, pp. 1503–1518, Jul. 2021.

[38] M. Schweizer and J. W. Kolar, "Design and implementation of a highly efficient three-level T-type converter for low-voltage applications," *IEEE Trans. Power Electron.*, vol. 28, no. 2, pp. 899–907, Feb. 2013.

[39] S. Wendel, A. Geiger, E. Liegmann, D. Arancibia, E. Durán, T. Kreppel, F. Rojas, F. Popp-Nowak, M. Diaz, A. Dietz, R. Kennel, and B. Wagner, "UltraZohm—A powerful real-time computation platform for MPC and multi-level inverters," in *Proc. IEEE Int. Symp. Pred. Control of Elect. Drives and Power Electron.*, Quanzhou, China, May/Jun. 2019, pp. 1–6.

Mattia Rossi (S'14 – M'22) received the B.Sc. and M.Sc. degrees in automation and control engineering from Politecnico di Milano, Milan, Italy, in 2013 and 2015, respectively. In 2021, he received the Ph.D. in electrical engineering from Politecnico di Milano, Milan, Italy, in collaboration with Tampere University, Tampere, Finland.

In 2015, he was with the ABB Ltd, Turgi, Switzerland, where he worked on the design of motor control strategies for medium-voltage drives. In 2019, he was a visiting Ph.D. student in the Chair of Electrical Drive Systems and Power Electronics, Technische Universität München, Munich, Germany. In 2021, he co-founded the ePEBB^s Srl, Italy. Since 2022, he is with the Faculty of Information Technology and Communication Sciences, Tampere University, Tampere, Finland, where he is currently a Postdoctoral Research Fellow. His main research activities cover model predictive control algorithms for power electronic-based systems and their embedded implementation, aiming to improve power conversion efficiency and system components reliability.

Dr. Rossi received the Best Student Paper Award at the 2019 IEEE International Symposium on Predictive Control of Electrical Drives and Power Electronics, the Student Paper and Travel Assistance (IES-SPTA) Award at the 2017 IEEE International Conference on Compatibility, Power Electronics and Power Engineering, and the Jorma Luomi Student Forum Award at the 2016 International Conference on Electrical Machines.

Petros Karamanakos (S'10 – M'14 – SM'19) received the Diploma and Ph.D. degrees in electrical and computer engineering from the National Technical University of Athens (NTUA), Athens, Greece, in 2007, and 2013, respectively.

From 2010 to 2011 he was with the ABB Corporate Research Center, Baden-Dättwil, Switzerland, where he worked on model predictive control strategies for medium-voltage drives. From 2013 to 2016 he was a PostDoc Research Associate in the Chair of Electrical Drive Systems and Power Electronics, Technische Universität München, Munich, Germany. Since 2016, he has been with the Faculty of Information Technology and Communication Sciences, Tampere University, Tampere, Finland, where he is currently an Associate Professor. His main research interests lie at the intersection of optimal control, mathematical programming and power electronics, including model predictive control and optimal modulation for power electronic converters and ac variable speed drives.

Dr. Karamanakos received the 2014 Third Best Paper Award of the IEEE Transactions on Industry Applications and two Prize Paper Awards at conferences. He serves as an Associate Editor of the IEEE Transactions on Industry Applications and of the IEEE Open Journal of Industry Applications.

Francesco Castelli-Dezza (M'89) received the M.Sc. and Ph.D. degrees in electrical engineering from Politecnico di Milano, Milan, Italy, in 1986 and 1990, respectively.

He is currently a Full Professor with the Department of Mechanical Engineering, Politecnico di Milano, Milan, Italy. In 2006, he co-founded the university spin-off MCM Srl, Italy, now NHOA Energy. In 2021, he co-founded the ePEBB^s Srl, Italy. His research interests include studies on dynamic behaviour of electrical machines, electrical drives control and design, and power electronics for energy flow management.

Prof. Castelli-Dezza is a member of the IEEE Industry Applications, Power Electronics, and Industrial Electronics societies.